Particle Induced Doublons in Strongly Correlated Systems

Bachelorarbeit
im 1-Fach-Bachelorstudiengang Physik
der Mathematisch-Naturwissenschaftlichen Fakultät
der Christian-Albrechts-Universität zu Kiel

vorgelegt von
Maximilian Rodriguez Rasmussen

Erstgutachter: Prof. Dr. Michael Bonitz
Zweitgutachter: Dr. Karsten Balzer

Kiel im August 2017

von Rodriguez Rasmussen, Maximilian
Particle Induced Doublons in Strongly Correlated Systems
Bachelorarbeit, Christian-Albrechts-Universität zu Kiel, 2017

Zusammenfassung

Das Hubbard-Modell sagt für stark korrelierte Systeme die Möglichkeit voraus, dass zwei Elektronen auf einem Gitterplatz ein Quasiteilchen, ein sogenanntes Doublon, formen, was zum erhalten der Doppelbesetzung führt. In dieser Arbeit wird der die Erzeugung von Doublons druch die Wechselwirkung mit einem geladenen Teilchen untersucht. Dazu wird mit numerisch exakten Methoden die Dynamik des Teilchens, das durch ein zweidimensionales hexagonales Gitter stößt, simuliert. Die Erzeugung stabiler Doppelbesetzung im System wird in Abhängigkeit von verschiedenen Parametern analysiert. Zum besseren Verständnis der Abläufe wird zudem zusätzlich ein vereinfachtes System betrachtet, das aus nur zwei Gitterpunkten besteht.

Summary

For strongly correlated system the Hubbard model predicts the possibility of the formation of a quasi-particle consisting of two electrons on the same site. These particles are called doublons. In this thesis production of such doublons on a two dimensional lattice system due interaction with a positively charged particle penetrating the lattice is analyzed. The dynamics and the doublon creation with regard key setup parameters are examined. To get a ground level understanding of the doublon formation, a simplified two site system additionally considered.

Contents

Chapter 1

Introduction

The interaction of condensed matter surfaces with particles is of high interest for research in plasma physics and condensed matter physics. Its examination is key to understanding plasma-surface effects that can change the properties of the solid, which is also very interesting for applications in material science. Therefore, a lot of effort has been devoted to theoretically describing this interaction ([28], [5], [3]) This task has, however, proven itself to be very difficult. Due to the complexity of condensed matter systems, elaborate theoretical models are needed, which require a lot of computing power. Through developments in in-situ experiments in plasma ([23], [15], [13]) and experiments with ultra cold lattices ([22], [26]), the actual dynamics might now become experimentally accessible.

The setup studied in this thesis consists of a two dimensional lattice penetrated by a positively charged projectile. Considering the lattice to be on the surface plane of a solid which is in contact with a plasma, this setup can be understood as a simplified model to examine the effects of the plasma's ions on the solid. To describe the lattice, the Hubbard model is used. This model has had great success since its introduction in 1963([11]).

Its main advantage over the popular single particle models for electrons in condensed matter is that correlation effects between the electrons are considered. This allows to describe systems in which correlation between the electrons has a substantial effect on their behaviour. One aspect of the Hubbard model is that two electrons on one lattice site in strongly correlated systems are predicted to form a quasi particle, called doublon, which leads to the number of doubly occupied sites being stable. This effect is particularly interesting, because the number of doubly occupied sites has a big influence on the electrical properties of the solid. In this thesis the possibility and extent of doublons being produced due to the charged projectile is examined.

The method used for the simulation presented in this thesis is so called exact propagation, wherein the Hamiltonian is diagonalized to obtain the groundstate and propagated in time using the time-dependent SchrÃ¶dinger equation. Therefore, the obtained results are numerically exact with regard to the used model. However with exact propagation only relatively small systems can be treated, because the number of basis states grows exponentially with the number of contained electrons ([8]).

The systems considered are 12-site two dimensional honeycomb-type lattices. The honeycomb lattice is very interesting, because there are real materials, like graphene, with this quasi two dimensional structure.These materials have received a lot of scientific attention in recent years (e.g. [20]). On those lattices the effect of particle induced doublons is studied.

The aim of this thesis is to provide a ground level examination of this effect. The projectile induced dynamics and the dependency of doublon production and stability on different simulation parameters, e.g. the projectile velocity, are studied. While the presented model is not in any way a complete description of plasma surface interaction, the examined effects could help to develop such a description. For example, the used model can be expanded later on to also cover other important effects, like ionization and multiple penetration. The results obtained from this thesis can serve as reference and basis to further develop the model, for example to examine larger systems.

In the beginning of this thesis, the theoretical background necessary is presented, including the Hubbard model, some numerical methods and the projectile interaction. In the next part the general setup and lattice structure considered for the simulations are discussed. Thereafter, the obtained results are shown and analyzed. In this section, the observed dynamics are presented and discussed. Following this section, the doublon production and its correlation with other quantities are examined. In order to do that, the setup is simulated and analyzed under varying extents of correlation, projectile velocity and starting position. Finally a simplified model is introduced to get a better ground level understanding of the events leading to the observed doublon production.

Chapter 2

Theory

In this chapter, the theoretical background needed in this thesis is presented. The first part introduces the basic principles of second quantization and the Hubbard model, which is used to theoretically describe the examined systems. The second part deals with the theoretical concept of exact propagation needed to understand the simulations done for this thesis. Additionally, the Lanctos algorithm, a numerical method used to compute the ground state, is presented.

2.1 Second quantization

The second quantization is a formalism used to describe many particle quantum systems. They are categorized by their occupation numbers of the single particle orbitals. To cover all possible particle numbers, one considers the direct sum of all N-particle Hilbert spaces $\mathcal{H}_N$, the so called Fock space:

$$\mathcal{F} = \bigoplus_{N \in \mathbb{N}} \mathcal{H}_N. \tag{2.1}$$

Any state in $\mathcal{F}$ can now be written as a linear combination of states of the form:

$$|\Psi\rangle = |n_1, n_2, n_3, ...\rangle \,. \tag{2.2}$$

Here n_i is the occupation number of the i-th orbital. The states are orthonormalized in a way that:

$$\langle \Psi | \Psi' \rangle = \prod_i \delta_{n_i, n_i'}. \tag{2.3}$$

If the orbitals are known, every information about the system is accessible with this representation. In second quantization any operator can be expressed via the creation- and annihilation operators $\hat{c}^\dagger$ and $\hat{c}$, which can be defined by their acting on an arbitrary state. For Fermions, in analogy to [6] and [25], they are given as:

$$\begin{aligned} \hat{c}_i^\dagger |..., n_i, ...\rangle &:= \sqrt{n_i + 1}\; (-1)^{a_i} |..., n_i + 1, ...\rangle \, \delta_{n_i,0}, & (2.4) \\ \hat{c}_i |..., n_i, ...\rangle &:= \sqrt{n_i}\; (-1)^{a_i} |..., n_i - 1, ...\rangle \, \delta_{n_i,1}, \quad a_i = \sum_{k<i} n_k. & (2.5) \end{aligned}$$

The creation operator $\hat{c}_i^\dagger$ increases the occupation number n_i by one. The annihilation operator $\hat{c}_i$ decreases n_i by one. The kronecker delta ensures that the Pauli principle is obeyed. The second prefactor a_i accounts for the anti-commutation relations between the operators:

$$\begin{aligned} \{\hat{c}_i^\dagger, \hat{c}_{i'}^\dagger\} &= \{\hat{c}_i, \hat{c}_{i'}\} = 0, && (2.6) \\ \{\hat{c}_i, \hat{c}_{i'}^\dagger\} &= \delta_{i,i'}. && (2.7) \end{aligned}$$

Using $\hat{c}_i^\dagger$ and $\hat{c}_i$, one can now define the occupation number operator for the i-th orbital n_i:

$$\begin{aligned} \hat{n}_i \left|..., n_i, ...\right\rangle &= \hat{c}_i^\dagger \hat{c}_i \left|..., n_i, ...\right\rangle \\ &= \sqrt{n_i}\,(-1)^{a_i}\,\hat{c}_i^\dagger \left|..., n_i - 1, ...\right\rangle \delta_{n_i,1} \\ &= n_i \left|..., n_i, ...\right\rangle. && (2.8) \end{aligned}$$

With these definitions for $\hat{c}$ and $\hat{c}^\dagger$, a single particle operator $\hat{B}_1$ acting on states in a system with N single particle orbitals becomes:

$$\hat{B}_1 = \sum_{i,j=1}^{N} \langle i|\,\hat{b}_1\,|j\rangle\,\hat{c}_i^\dagger \hat{c}_j = \sum_{i,j=1}^{N} b_{ij} \hat{c}_i^\dagger \hat{c}_j, \tag{2.9}$$

where b_{ij} is the respective matrix element of the operator $\hat{B}_2$. Any two particle operators in such a system $\hat{B}_2$ can then be expressed in the following way:

$$\hat{B}_2 = \frac{1}{2!} \sum_{i,j,k,l=1}^{N} \langle ij|\,\hat{b}_2\,|kl\rangle\,\hat{c}_i^\dagger \hat{c}_j^\dagger \hat{c}_l \hat{c}_k = \frac{1}{2} \sum_{i,j,k,l=1}^{N} b_{ijkl} \hat{c}_i^\dagger \hat{c}_j^\dagger \hat{c}_l \hat{c}_k, \tag{2.10}$$

where the ordering of creation and annihilation operators is due to their anti-commutation relations. A Hamiltonian, consisting of the single particle operator for the kinetic energy and an external potential $\hat{T}$ and the two particle operator $\hat{W}$ for the interaction between the particles, becomes:

$$\hat{H} = \sum_{i,j=1}^{N} t_{ij} \hat{c}_i^\dagger \hat{c}_j + \frac{1}{2} \sum_{i,j,k,l=1}^{N} w_{ijkl} \hat{c}_i^\dagger \hat{c}_j^\dagger \hat{c}_l \hat{c}_k, \tag{2.11}$$

where the coefficients t_{ij} and w_{ijkl} can be computed as the matrix elements of the respective operators in space representation (see [12]). Assuming a distance dependent potential like the Coulomb-Interaction, they can be calculated as:

$$\begin{aligned} t_{ij} &= \int d^3\vec{r}\;\Phi_i^*(\vec{r}) \left(-\frac{\hbar^2 \nabla^2}{2m} + v(\vec{r})\right) \Phi_j(\vec{r}), && (2.12) \\ w_{ijkl} &= \int d^3\;\vec{r} d^3\vec{r}' \Phi_i^*(\vec{r}) \Phi_j^* \vec{r}' V(|\vec{r} - \vec{r}'|) \Phi_k(\vec{r}) \Phi_l(\vec{r}'). && (2.13) \end{aligned}$$

2.2 The Hubbard model

The Hubbard Model is a simple approximation for condensed matter systems. It is the simplest many particle model that can not be reduced to a single particle theory ([1]). However, a lot of valuable and very interesting results have been obtained with this approach in the field of condensed matter physics ([24], [10]). It has been applied successfully to understand ferromagnetism, superconductivity, etc.

In the Hubbard model, the solid state system is approximated by a static lattice structure for the atomic cores. The electrons are assumed to be found in orbitals dislocated around the lattice position of the cores. In second quantization the Hamiltonian then is of the form eq. 2.11.

The following assumptions are made in the Hubbard model: t_{ij} is assumed to be zero when i and j are not nearest neighbors and a constant value $-J$ whenever they are. This assumption makes sense for tightly bound electrons, where the Φ_i's in 2.12 can be assumed to be Fourier-transformed Bloch-functions, so called Wannier functions. This leads to the overlap in 2.12 being small for non nearest neighbors. The on-site terms t_{ii} are neglected, because they may be absorbed into to the chemical potential in a grand canonical model [10].

Because of the screening due to the electric field of the cores, interaction between electrons is only taken into account if they are on the same site. Therefore, in the interaction term two electrons on the same lattice site contribute the value U to the energy, while electrons on different lattice sites do not contribute to the energy.

Under those assumptions the Hubbard Hamiltonian has a much simpler form and can be written as:

$$\hat{H} = \hat{T} + \hat{W} = -J \sum_{\langle i,j \rangle,\alpha} \hat{c}^{\dagger}_{i\alpha}\hat{c}_{j\alpha} + U \sum_{i} \hat{n}_{i\uparrow}\hat{n}_{i\downarrow}. \tag{2.14}$$

The first term $\hat{T}$ is called the hopping term, where one electron with spin α on site j is destroyed and one is created on site i. As a consequence of electrons never changing spin when hopping, $\hat{H}$ commutes with the total number operator for $\uparrow$-electrons $\hat{N}_{\uparrow}$ and the number operator for $\downarrow$-electrons $\hat{N}_{\downarrow}$. Thus the number of $\uparrow$-electrons and $\downarrow$-electrons cannot change. The $< i, j >$-symbol signifies that only nearest-neighbor-indices are considered in the sum. The prefactor J is called the hopping constant. The second term $\hat{W}$ represents the on-site interaction with the so called interaction strength, U. All properties of the Hamiltonian are contained in the lattice structure and the relative interaction strength U/J.

2.2.1 The non interacting case

For the non interacting case the Hubbard Hamiltonian can be solved with low effort in momentum space. For simplicity, the one dimensional case is treated. For $U = 0$ the Hubbard Hamiltonian then becomes:

$$\hat{H} = -J \sum_{<i,j>,\alpha} \hat{c}^{\dagger}_{i\alpha}\hat{c}_{j\alpha}. \tag{2.15}$$

To Fourier transform this Hamiltonian, the expressions for $\hat{c}$ and $\hat{c}^\dagger$ in momentum representation are needed:

$$\begin{aligned}
\hat{c}^\dagger_{m\alpha} &= \frac{1}{\sqrt{N}} \sum_k \mathrm{e}^{-\mathrm{i}km} \hat{\hat{c}}^\dagger_{k\alpha}, && (2.16) \\
\hat{c}_{m\alpha} &= \frac{1}{\sqrt{N}} \sum_k \mathrm{e}^{\mathrm{i}km} \hat{\hat{c}}_{k\alpha}. && (2.17)
\end{aligned}$$

where N is the total number of sites in the system. On a finite lattice the momentum k has discrete values $k_i = \frac{2\pi i}{N}$, with $i \in \{0, 1, ..., N\}$. $\hat{\hat{c}}^\dagger_{k\alpha}$ and $\hat{\hat{c}}_{k\alpha}$ are the creation- and annihilation operators in momentum space, which create or annihilate an electron with momentum k and spin α. Inserting these expressions in 2.15 leads to:

$$\begin{aligned}
\hat{H} &= -J \sum_{<m,n>,\alpha} \hat{c}^\dagger_{m\alpha}\hat{c}_{n\alpha} = -\frac{J}{N} \sum_{<m,n>,\alpha} \sum_{k,k'} \mathrm{e}^{-\mathrm{i}km} \hat{\hat{c}}^\dagger_{k\alpha} \mathrm{e}^{\mathrm{i}k'n} \hat{\hat{c}}_{k\alpha} \\
&= -\frac{J}{N} \sum_m \left(\mathrm{e}^{-\mathrm{i}km} \mathrm{e}^{\mathrm{i}k'(m+1)} + \mathrm{e}^{-\mathrm{i}km} \mathrm{e}^{\mathrm{i}k'(m-1)} \right) \sum_{k,k',\alpha} \hat{\hat{c}}^\dagger_{k\alpha} \hat{\hat{c}}_{k\alpha} \\
&= -J \sum_{k,k',\alpha} \hat{\hat{c}}^\dagger_{k\alpha} \hat{\hat{c}}_{k\alpha} \left(\mathrm{e}^{\mathrm{i}k'} + \mathrm{e}^{-\mathrm{i}k'} \right) \frac{1}{N} \sum_m \mathrm{e}^{-\mathrm{i}(k'-k)m} \\
&= -J \sum_{k,k',\alpha} \hat{\hat{c}}^\dagger_{k\alpha} \hat{\hat{c}}_{k\alpha} 2\cos\, k'\ \delta_{k',k} = \sum_{k,\alpha} -2J\cos\, k\ \hat{n}_{k\alpha} && (2.18)
\end{aligned}$$

As one can see, the Hamiltonian becomes diagonal in momentum representation. The dispersion relation is $\epsilon_k = -2J\cos k$. One can thus see any electron in this case has an energy between $-2J$ and $+2J$.

For $U \neq 0$ however, the Hubbard Hamiltonian cannot be solved analytically by just transforming into momentum space. For large U the Hamiltonian can be transformed and the effective doublon Hamiltonian can be derived, which leads to double occupation being preserved for large U in small systems. This allows the definition of doublons.

2.2.2 Effective doublon Hamiltonian

In this section, the effective doublon Hamiltonian is derived. For large U/J the behaviour of states with high double occupation is examined. This is done in analogy to [16]. To treat the behaviour of doubly occupied states, first, the hole operator $\hat{h}_{i\alpha} = \hat{1} - \hat{n}_{i\alpha}$ is defined, which returns the number of holes at lattice site i with spin α. Now the hopping term $\hat{T}$ of the Hamiltonian can be rewritten using the relation $\hat{1} = \hat{h}_{i\alpha} + \hat{n}_{i\alpha}$:

$$\hat{T} = -J \sum_{<i,j>,\alpha} \hat{1}\ \hat{c}^\dagger_{i\alpha}\hat{c}_{j\alpha}\ \hat{1} \qquad (2.19)$$

$$\begin{aligned} &= -J \sum_{<i,j>,\alpha} \left(\hat{h}_{i\alpha} + \hat{n}_{i\alpha}\right) \hat{c}^{\dagger}_{i\alpha} \hat{c}_{j\alpha} \left(\hat{h}_{j\alpha} + \hat{n}_{j\alpha}\right) \\ &= \hat{T}_0 + \hat{T_{-1}} + \hat{T}_1, \end{aligned}$$

with:

$$\hat{T}_{-1} := -J \sum_{<i,j>,\alpha} \hat{h}_{i\alpha} \hat{c}^{\dagger}_{i\alpha} \hat{c}_{j\alpha} \hat{n}_{j\alpha}, \tag{2.20}$$

$$\hat{T}_0 := -J \sum_{<i,j>,\alpha} \hat{n}_{i\alpha} \hat{c}^{\dagger}_{i\alpha} \hat{c}_{j\alpha} \hat{n}_{j\alpha} + \hat{h}_{i\alpha} \hat{c}^{\dagger}_{i\alpha} \hat{c}_{j\alpha} \hat{h}_{j\alpha}, \tag{2.21}$$

$$\hat{T}_1 := -J \sum_{<i,j>,\alpha} \hat{n}_{i\alpha} \hat{c}^{\dagger}_{i\alpha} \hat{c}_{j\alpha} \hat{h}_{j\alpha}. \tag{2.22}$$

$$\tag{2.23}$$

It is easy to see that the number of doubly occupied sites is lowered by $\hat{T}_{-1}$, increased by $\hat{T}_1$ and unchanged by $\hat{T}_0$. For $m \in \{-1, 0, 1\}$ one gets the relations:

$$\left[\hat{V}, \hat{T}_m\right] = mU\hat{T}_m, \tag{2.24}$$

$$\hat{T}_i^{\dagger} = \hat{T}_{-i}. \tag{2.25}$$

Thus the Transformation

$$\hat{H}' = \mathrm{e}^{\mathrm{i}\hat{S}} \hat{H} \mathrm{e}^{-\mathrm{i}\hat{S}} = \hat{H} + \frac{\left[\mathrm{i}\hat{S}, \hat{H}\right]}{1!} + \frac{\left[\mathrm{i}\hat{H}, \left[\mathrm{i}\hat{S}, \hat{H}\right]\right]}{2!} + \ldots, \tag{2.26}$$

using

$$\hat{S} = -\frac{i}{U}\left(\hat{T}_1 - \hat{T}_{-1}\right) \tag{2.27}$$

is unitary, because $\hat{S}$ is self-adjoint due to 2.25; and in first order with 2.24 the Hamiltonian becomes:

$$\hat{H'}^{(1)} = \hat{T}_0 + \hat{V} + \frac{1}{U}\left(\left[\hat{T}_1, \hat{T}_{-1}\right] + \left[\hat{T}_0, \hat{T}_{-1}\right] + \left[\hat{T}_1, \hat{T}_0\right]\right) + \mathcal{O}(U^{-2}). \tag{2.28}$$

From this equation it can already be seen that for large U/J the number of doubly occupied sites is preserved in the Hubbard model. Therefore, the two electrons in a doubly occupied site can be viewed as a unit, this quasi particle is called a doublon. By neglecting the $\mathcal{O}(U^{-2})$-terms one can now derive the effective doublon Hamiltonian which governs the behaviour of doublons ([16]):

$$\hat{H}_{doub} = \frac{J^2}{U} \sum_{<i,j>} \hat{d}^{\dagger}_i \hat{d}_j + \sum_{i,j} V_{ij} \hat{n}^d_i \hat{n}^d_j, \tag{2.29}$$

where $\hat{d}^{\dagger}_i = \hat{c}^{\dagger}_{i\uparrow} \hat{c}^{\dagger}_{i\downarrow}$ is the creation operator , $\hat{d}_i = \hat{c}_{i\uparrow} \hat{c}_{i\downarrow}$ is the annihilation operator and $\hat{n}^d_i = \hat{d}^{\dagger}_i \hat{d}_i$ is the occupation number operator for doublons. $V_{ij} = \infty$ for $i = j$ because of the Pauli principle and $V_{ij} = -\frac{J^2}{U}$ if i and j are nearest neighbors else $V_{ij} = 0$. Using this model the dynamics of doublons have been successfully examined ([17], [4]).

2.2.3 Hubbard dimer

Generally, the Hubbard Hamiltonian can not be solved analytically for $U \neq 0$. For a two site system however, an analytical solution can be found by diagonalizing the Hamiltonian. Because the Hamiltonian doesn't change the total number of spin-up and spin-down electrons, this section only concentrates on the half filled case with two electrons in the system. In this case, the Hamiltonian can be written in matrix form with the four basis states:

$$\begin{aligned}
|\Psi_1\rangle &= |\uparrow,\downarrow\rangle = \hat{c}^\dagger_{2\downarrow}\hat{c}^\dagger_{1\uparrow}|0\rangle\,, \\
|\Psi_2\rangle &= |\downarrow,\uparrow\rangle = \hat{c}^\dagger_{1\downarrow}\hat{c}^\dagger_{2\uparrow}|0\rangle\,, \\
|\Psi_3\rangle &= |\downarrow\uparrow,-\rangle = \hat{c}^\dagger_{1\downarrow}\hat{c}^\dagger_{1\uparrow}|0\rangle\,, \\
|\Psi_4\rangle &= |-,\downarrow\uparrow\rangle = \hat{c}^\dagger_{2\downarrow}\hat{c}^\dagger_{2\uparrow}|0\rangle\,.
\end{aligned}$$

In this basis $\hat{H}$ becomes (see [21]):

$$H = \begin{pmatrix} 0 & 0 & -J & -J \\ 0 & 0 & J & J \\ -J & J & U & 0 \\ -J & J & 0 & U, \end{pmatrix} \tag{2.30}$$

where the sign of the J-elements is due to the commutation relations of the operators in 2.6 and 2.7. This 4×4 matrix can be diagonalized analytically by solving the characteristic polynomial and then calculating the eigenvectors or rewriting $\hat{H}$ in another basis representation which uses the symmetry of the Hubbard Hamiltonian. This leads to the eigenvalues and their respective eigenvectors:

$$\begin{aligned}
E^- &= \frac{U}{2} - \frac{\sqrt{U^2+16J^2}}{2}, \quad |\Psi^-\rangle = \frac{(-|\Psi_1\rangle + |\Psi_2\rangle) + \frac{E^-}{2J}(|\Psi_3\rangle + |\Psi_4\rangle)}{\sqrt{2+\left(\frac{E^-}{\sqrt{2}J}\right)^2}}, \\
E^+ &= \frac{U}{2} + \frac{\sqrt{U^2+16J^2}}{2}, \quad |\Psi^+\rangle = \frac{(|\Psi_2\rangle - |\Psi_1\rangle) + \frac{E^+}{2J}(|\Psi_3\rangle + |\Psi_4\rangle)}{\sqrt{2+\left(\frac{E^+}{\sqrt{2}J}\right)^2}}, \\
E^0 &= 0, \quad |\Psi^0\rangle = \frac{|\Psi_1\rangle + |\Psi_2\rangle}{\sqrt{2}}, \\
E^U &= U, \quad |\Psi^U\rangle = \frac{|\Psi_4\rangle - |\Psi_3\rangle}{\sqrt{2}}.
\end{aligned} \tag{2.31}$$

The eigenvalues' dependency on U/J is illustrated in 2.1. For large U/J E^+ approaches E^U and E^- approaches E^0. For large U/J the gap between these two pairs of eigenenergies is called the Hubbard gap. The eigenenergies E^- and

E^0 are in the so called lower Hubbard band and E^U and E^+ are in the upper Hubbard band of the dimer.

For this simple system, it is easy to see that for $U/J > 2$ any doublon has an infinite lifespan, because its interaction energy of $2t$ cannot be dissipated in the two site system. The stability of doublons and the doublon Hamiltonian, which predicts its dynamics and behaviour on big systems, are both consequences of the problem in energy dissipation for doubly occupied states.

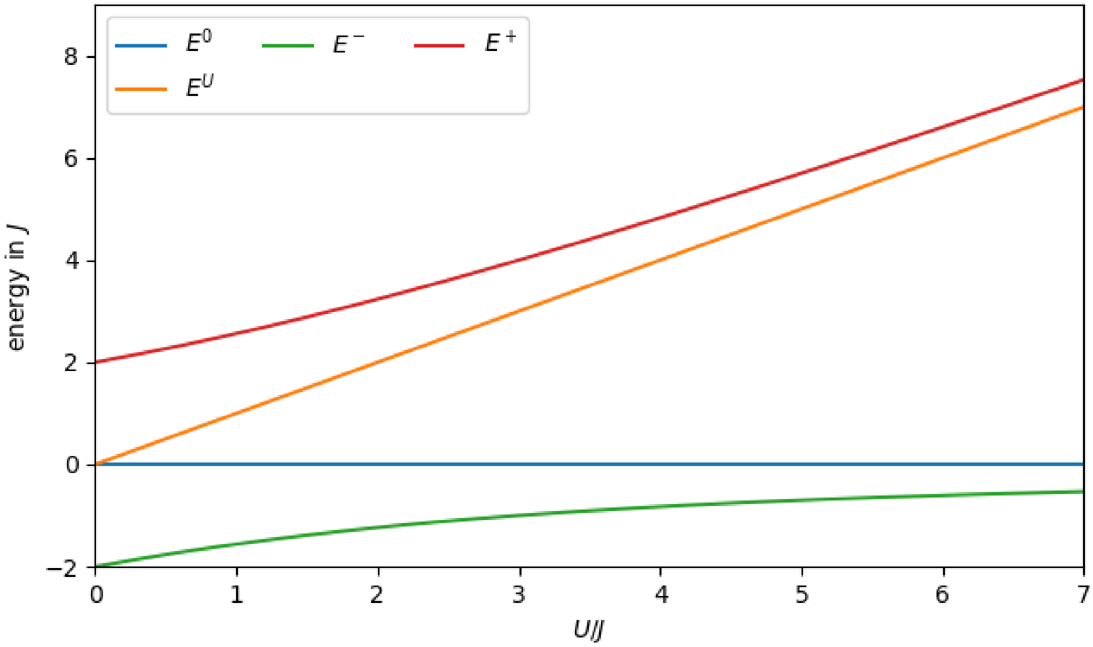

Figure 2.1: Energy eigenvalues in units of J of the Hubbard dimer as a function of the relative interaction strength U/J

2.3 Exact propagation

In this section, the theoretical background for the specific simulation is presented. At the start of the simulation, the ground state is computed by diagonalizing the Hamiltonian, so the ground state is numerically exact. The problem with the diagonalization of the Hubbard Hamiltonian is the huge basis dimension even at a few sites. This makes all matrix-vector-operations extensive and leads to high memory consumption when saving the large matrices and vectors. Therefore, a numerical treatment that approximates the ground sate but drastically reduces computational effort and memory usage is needed. To maximize the size of systems possibly observable with this method, the needed computational effort and memory usage had to be reduced. To this end the Lanczos method was used to diagonalize the Hamiltonian. This algorithm is presented below. The calculated ground state is then propagated in time with the time-dependent SchrÃ¶dinger equation (TDSE).

2.3.1 Lanczos Method

The Lanczos algorithm can be used to approximate the eigenvalues and eigenvectors of an arbitrary N-dimensional self-adjoint matrix H. The algorithm commutes a tridiagonal M-dimensional matrix T, the eigenvalues and eigenvectors of which approximate those of H. The description of the Lanczos algorithm is done in analogy to [18].

The algorithm starts with an arbitrary normalized vector $|\Psi_0\rangle \neq 0$ that is not to be an eigenvector of H. Then from $|\Psi_0\rangle$ M vectors Ψ_i are computed recursively through $|\Psi_{-1}\rangle = |0\rangle$:

$$\left|\Psi'_{i+1}\right\rangle = H\left|\Psi_i\right\rangle - a_i\left|\Psi_i\right\rangle - b_i\left|\Psi_{i-1}\right\rangle, \tag{2.32}$$

where $a_i = \langle\Psi_i| H |\Psi_i\rangle$ and $b_i = \langle\Psi_{i-1}| H |\Psi_i\rangle$. Now $|\Psi_{i+1}\rangle$ is computed by normalizing $|\Psi'_i\rangle$:

$$|\Psi_{i+1}\rangle = \frac{\left|\Psi'_{i+1}\right\rangle}{\sqrt{\left\langle\Psi'_{i+1}\middle|\Psi'_{i+1}\right\rangle}}. \tag{2.33}$$

One can see that this set of M vectors is orthogonal through mathematical induction:

Base case for n = 1 vectors: Trivially, the set is orthogonal when only consisting of one vector $|\Psi_0\rangle \neq |0\rangle$.

Induction step: Assume that $|\Psi_0\rangle, ..., |\Psi_n\rangle$ are orthogonal. Now $\left|\Psi'_{n+1}\right\rangle$ is orthogonal to all previous vectors:

$$\begin{aligned}
\langle\Psi_n|\Psi_{n+1}\rangle &= \frac{1}{\sqrt{\left\langle\Psi'_{n+1}\middle|\Psi'_{n+1}\right\rangle}}\left(\langle\Psi_n| H |\Psi_n\rangle - a_n\langle\Psi_n|\Psi_n\rangle - b_n\langle\Psi_n|\Psi_{n-1}\rangle\right) \\
&= \frac{1}{\sqrt{\left\langle\Psi'_{n+1}\middle|\Psi'_{n+1}\right\rangle}}\left(\langle\Psi_n| H |\Psi_n\rangle - \langle\Psi_n| H |\Psi_n\rangle - 0\right) \\
&= 0
\end{aligned} \tag{2.34}$$

also

$$\begin{aligned}
\langle\Psi_{n-1}|\Psi_{n+1}\rangle &= \frac{1}{\sqrt{\left\langle\Psi'_{n+1}\middle|\Psi'_{n+1}\right\rangle}}\left(\langle\Psi_{n-1}| H |\Psi_n\rangle - a_n\langle\Psi_{n-1}|\Psi_n\rangle - b_n\langle\Psi_{n-1}|\Psi_{n-1}\rangle\right) \\
&= \frac{1}{\sqrt{\left\langle\Psi'_{n+1}\middle|\Psi'_{n+1}\right\rangle}}\left(\langle\Psi_{n-1}| H |\Psi_n\rangle - 0 - \langle\Psi_{n-1}| H |\Psi_n\rangle\right) \\
&= 0
\end{aligned} \tag{2.35}$$

and for $i < n-1$ we get:

$$\begin{aligned}\langle\Psi_i|\Psi_{n+1}\rangle &= \frac{1}{\sqrt{\langle\Psi'_{n+1}|\Psi'_{n+1}\rangle}}\left(\langle\Psi_i|H|\Psi_n\rangle - a_n\langle\Psi_i|\Psi_n\rangle - b_n\langle\Psi_i|\Psi_{n-1}\rangle\right)\\ &= \frac{\langle\Psi_i|H|\Psi_n\rangle}{\sqrt{\langle\Psi'_{n+1}|\Psi'_{n+1}\rangle}}. \end{aligned} \tag{2.36}$$

H is hermitian, this yields:

$$\begin{aligned}\langle\Psi_i|H|\Psi_n\rangle &= \left(\langle\Psi'_{i+1}| + a_i\langle\Psi_i| + b_i\langle\Psi_{i-1}|\right)|\Psi_n\rangle\\ &= \langle\Psi'_{i+1}|\Psi_n\rangle + a_i\langle\Psi_i|\Psi_n\rangle + b_i\langle\Psi_{i-1}|\Psi_n\rangle\\ &= 0. \end{aligned} \tag{2.37}$$

Thus $\langle\Psi_i|\Psi_{n+1}\rangle = 0$ and the orthogonality is shown via mathematical induction.

Furthermore, it can be seen that H becomes tridiagonal in the Lanczos basis, because of:

$$\begin{aligned}H|\Psi_n\rangle &= |\Psi'_{n+1}\rangle + a_n|\Psi_n\rangle + b_n|\Psi_{n-1}\rangle\\ &= b_{n+1}|\Psi_{n+1}\rangle + a_n|\Psi_n\rangle + b_n|\Psi_{n-1}\rangle. \end{aligned} \tag{2.38}$$

With the transformation matrix $S = (|\Psi_0\rangle \ldots |\Psi_{M-1}\rangle)$ H becomes:

$$T = S^\dagger H S = \begin{pmatrix} a_0 & b_1 & . & . & . & 0\\ b_1 & a_1 & b_2 & & & .\\ . & b_2 & . & & & .\\ . & & & . & b_{M-2} & .\\ . & & & b_{M-2} & a_{M-2} & b_{M-1}\\ 0 & . & . & . & b_{M-1} & a_{M-1} \end{pmatrix}. \tag{2.39}$$

The eigenvalues of the M-dimensional matrix T can now be computed using methods like QR decomposition. For $M = N$ calculated vectors, the Matrix T is similar to H, thus the eigenvalues of T are also eigenvalues of H and for any eigenstate $|x\rangle$ of T the state $|y\rangle = S|x\rangle$ is an eigenstate of H. For $M < N$ the extreme eigenvalues get approximated the fastest (see [9] and [18]). In practice, the dimension of the Lanczos basis is much smaller than the dimension of H. For ground state calculations good results can be achieved with M around 100. For the results presented in this thesis, M was set to 300. The main advantage of this method is that the actual calculation of the eigenvalues and -vectors is done on the relatively small matrix T. The computing of the Lanczos basis has the complexity of $\mathcal{O}(m \cdot N^2)$, whereas QR-decomposition is $\mathcal{O}(N^3)$ [9].

2.3.2 Time Propagation

The Dynamics of any quantum mechanical system are governed by the time-dependent SchrÃ¶dinger equation:

$$\mathrm{i}\hbar\frac{\partial}{\partial t}\left|\psi\right\rangle = \hat{H}\left|\Psi\right\rangle \tag{2.40}$$

Thus the system can be propagated using the time-evolution operator $\hat{U}(t, t_0)$:

$$\left|\Psi(t)\right\rangle = \hat{U}(t, t_0)\left|\Psi(t_0)\right\rangle, \tag{2.41}$$

with

$$\hat{U}(t, t_0) = \mathrm{e}^{-\frac{\mathrm{i}}{\hbar}\int_{t_0}^{t}\hat{H}(t')dt'}. \tag{2.42}$$

For small time steps Δt, the Hamiltonian is assumed to be constant. Thus the time propagation can be done with:

$$\left|\Psi(t+\Delta t)\right\rangle = \mathrm{e}^{-\frac{\mathrm{i}}{\hbar}\hat{H}(t)\Delta t}\left|\Psi(t)\right\rangle, \tag{2.43}$$

where the exponential function is approximated by its Taylor polynomial. For $\lim\limits_{\Delta t\to 0}$, this method of time propagation would still be exact. Due to numerical limitations in choosing the time step and evaluating the exponential function, however, it becomes less accurate the longer the system is propagated in time. In the simulations done for this thesis, the time step is variable, becoming smaller the more the Hamiltonian changes to optimize the usage of computational capacities.

2.4 Landau-Zener effect

The Landau-Zener effect describes non-adiabatic transitions at an avoided crossing of linearly traversed energy levels. This presentation follows Rubbmark et al. [19]. Consider an unperturbed Hamiltonian $\hat{H}_0$ with the eigenstates $\left|1\right\rangle$ and $\left|2\right\rangle$. With both $\hat{H}_0$ and the eigenvalues E_1 and E_2, but not the eigenstates, depending on some parameter q one gets:

$$\hat{H}_0(q)\left|1\right\rangle = E_1\left|1\right\rangle, \tag{2.44}$$

$$\hat{H}_0(q)\left|2\right\rangle = E_2\left|2\right\rangle. \tag{2.45}$$

The unperturbed eigenenergies are assumed to have the form shown in fig. 2.2, where they degenerate for some value of q and vary linearly around this crossing.

Now a perturbation is considered that breaks the degeneracy at the crossing. With a perturbation $\hat{V}$, that is supposed to be independent of q, the Hamiltonian can be written as:

$$\hat{H}(q) = \hat{H}_0(q) + \hat{V}. \tag{2.46}$$

Using the basis states $\left|1\right\rangle$ and $\left|2\right\rangle$, $\hat{H}$ can be written in matrix form and becomes

$$H = \begin{pmatrix} \epsilon_1(q) & \frac{1}{2}E_0\mathrm{e}^{\mathrm{i}\Phi} \\ \frac{1}{2}E_0\mathrm{e}^{\mathrm{i}\Phi} & \epsilon_2(q) \end{pmatrix}, \tag{2.47}$$

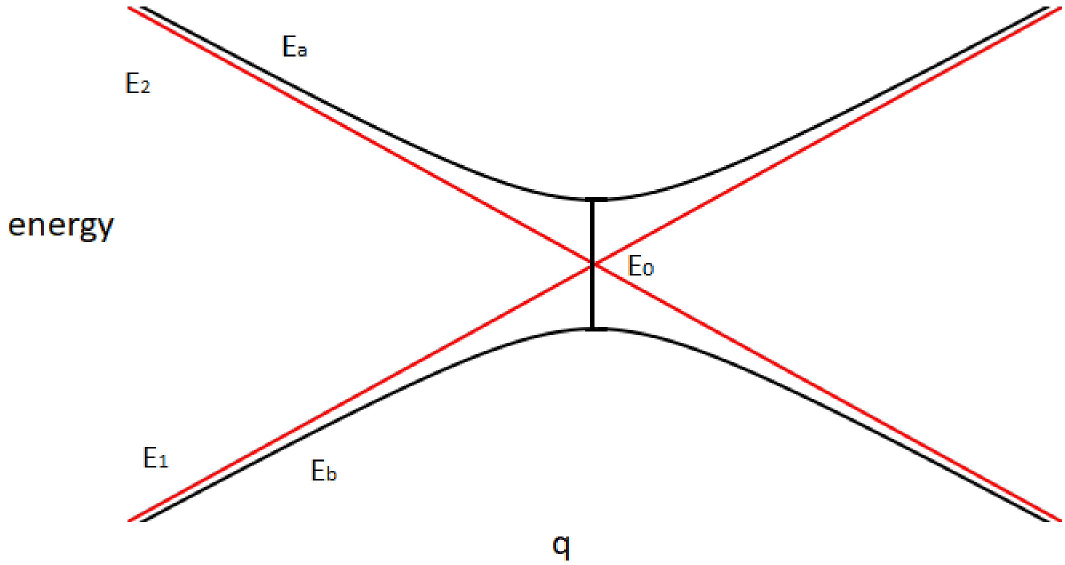

Figure 2.2: Eigenenergies of the unperturbed system (red) E_1, E_2 and the perturbed system (black) E_a, E_b as a function of the parameter q. The unperturbed eigenenergies are assumed to linearly depend on q. The energy gap at the avoided crossing is $E_0 = 2|\langle 1|\hat{V}|2\rangle|$.

where

$$\epsilon_1(q) = E_1(q) + \langle 1|\hat{V}|1\rangle , \tag{2.48}$$

$$\epsilon_2(q) = E_2(q) + \langle 2|\hat{V}|2\rangle , \tag{2.49}$$

$$\langle 1|\hat{V}|2\rangle = \frac{1}{2}E_0 \mathrm{e}^{\mathrm{i}\Phi}, 0 \leq \Phi \leq 2\pi. \tag{2.50}$$

The eigenenergies now are

$$E_a(q) = \frac{1}{2}\left((E_1 + E_2) + \sqrt{E(q)^2 + E_0^2}\right) , \tag{2.51}$$

$$E_b(q) = \frac{1}{2}\left((E_1 + E_2) - \sqrt{E(q)^2 + E_0^2}\right) , \tag{2.52}$$

with $E(q) = E_1(q) - E_2(q)$, which becomes $E(q) = const. \cdot q$ in the vicinity of the crossing. The respective eigenvectors are

$$|a\rangle(q) = \cos\left(\frac{\Theta(q)}{2}\right) \mathrm{e}^{-\mathrm{i}\frac{\Phi}{2}} |1\rangle + \sin\left(\frac{\Theta(q)}{2}\right) \mathrm{e}^{\mathrm{i}\frac{\Phi}{2}} |2\rangle , \tag{2.53}$$

$$|b\rangle(q) = -\sin\left(\frac{\Theta(q)}{2}\right) \mathrm{e}^{-\mathrm{i}\frac{\Phi}{2}} |1\rangle + \cos\left(\frac{\Theta(q)}{2}\right) \mathrm{e}^{\mathrm{i}\frac{\Phi}{2}} |2\rangle , \tag{2.54}$$

with $\tan\Theta(q) = \frac{E_0}{E(q)}$. To describe the possible transition, the most important quantities are the energy difference $\Delta E = E_0$ at the avoided crossing and its width

$$q_0 = \frac{E_0}{\left|\frac{dE}{dt}\right|}. \tag{2.55}$$

To calculate the dynamics of the full Hamiltonian, the TDSE has to be solved:

$$i\hbar\frac{\partial}{\partial t}\left|\psi\right\rangle = \hat{H}\left|\Psi\right\rangle. \tag{2.56}$$

An arbitrary state $\left|\Psi\right\rangle(t)$ can be written in the basis of $|1\rangle$ and $|2\rangle$:

$$\left|\Psi(t)\right\rangle = C_1(t)\mathrm{e}^{\mathrm{i}\int_t^0}E_1dt'\left|1\right\rangle + C_2(t)\mathrm{e}^{\mathrm{i}\int_t^0}E_2dt'\left|2\right\rangle. \tag{2.57}$$

Substituting this into the TDSE and using the definitions of eq 2.48 leads to the decoupled equations

$$\ddot{C}_1(t) - \frac{\text{ß}}{\hbar}E(t)\dot{C}_1 + \frac{E_0^2}{4}C_1 = 0, \ddot{C}_2(t) + \frac{\text{ß}}{\hbar}E(t)\dot{C}_2 + \frac{E_0^2}{4}C_2 = 0. \tag{2.58}$$

Now the case of q depending linearly on time and thus $E(t) = \alpha t$ is considered. Given a system prepared in state $|a\rangle$, the probability of a transition into $|b\rangle$ then becomes

$$P_{ab} = \mathrm{e}^{-\frac{2\pi}{\hbar}E_0q_0} = \mathrm{e}^{-\frac{2\pi}{\hbar}\frac{E_0^2}{|\alpha|}}. \tag{2.59}$$

This probability is now only dependent on the energy gap at the avoided crossing and the gradient of the energy difference.

2.5 Projectile interaction

In the simulation a positively charged projectile with charge q and a fixed starting velocity vertically penetrates a two dimensional lattice, also see Balzer, SchlÃ¼nzen, and Bonitz [3]). Because all simulations consider a half filled lattice, the lattice as a whole is neutrally charged. While the position of the atomic cores on the lattice are assumed to be fixed, the dynamic of the electrons is strongly influenced by the electric field induced by the projectile. The interaction between the projectile and an electron on site i is assumed to be the Coulomb potential:

$$W_{ii}(t) = -\frac{eq}{4\pi\epsilon_0}\frac{1}{|\vec{r}_p(t) - R_i|}, \tag{2.60}$$

where $\vec{r}_p(t)$ is the current projectile position and R_i is the position of the site the electron is on. Because the electrons are considered to be localized on the sites, it is clear that for $i \neq j$ $W_{ij}(t) = 0$. This single particle term has to be added to the Hamiltonian from eq. 2.14. Using eq. 2.9 the Hamiltonian now reads:

$$\hat{H}(t) = -J\sum_{\langle i,j\rangle,\alpha}\hat{c}_{i\alpha}^{\dagger}\hat{c}_{j\alpha} + U\sum_i\hat{n}_{i\uparrow}\hat{n}_{i\downarrow} + \sum_i W_{ii}(t)\left(\hat{n}_{i\uparrow} + \hat{n}_{i\downarrow}\right). \tag{2.61}$$

To calculate the retroactive effect of the lattice on the projectile, the classical equation of motion is used:

$$\vec{F}(t) = \nabla W(t) = \nabla \left(\sum_i \frac{eq}{4\pi\epsilon_0} \frac{1}{|\vec{r}_p(t) - R_i|} \left(2 - \hat{n}_{i\uparrow} - \hat{n}_{i\downarrow}\right) \right) = m_p \ddot{\vec{r}}. \tag{2.62}$$

The projectile then gets propagated by solving this equation for discrete time values at intervals of the small time step Δt:
By calculating the acceleration $\vec{a}(t) = \ddot{\vec{r}}(t)$, the velocity $\vec{v}$ can be computed for the next time step. Advancing one time step, $\vec{r}(t + \Delta t)$ can be computed by averaging over the velocity:

$$\vec{r}(t + \Delta t) = \vec{r}(t) + \frac{\vec{v}(t) + \vec{v}(t + \Delta t)}{2} \Delta t. \tag{2.63}$$

Chapter 3

Model and setup

For this thesis, small honeycomb systems with a 12-site lattice are simulated to understand the projectile induced doublons. The dynamical evolution of the double occupation and density on the different lattice sites is accessible through exact propagation. With this setup, the dependency of the induced double occupation on projectile velocity and interaction strength is studied.

All simulations are done at half filling, i.e. with 12 electrons in the 12-site model. Also, the total number of ↑-electrons and ↓-electrons is the same for all considered systems. As mentioned in 2.2 these numbers cannot change, when using the Hubbard model. Thus the number D of basis states for the Hubbard Hamiltonian with N sites becomes:

$$D = \binom{N}{\frac{N}{2}} \cdot \binom{N}{\frac{N}{2}}, \tag{3.1}$$

The hopping constant for the Hubbard Hamiltonian is set to $J = 1eV$, while the relative interaction strength U/J is varied to study the importance of correlation effects on the induced doublons. The value $J = 1eV$ is not chosen with the aim to simulate any specific real material, nevertheless this value is chosen to be realistic. In comparison, the hopping amplitude for graphene is $J_{\text{graphene}} = 2.8eV$ and for silicene it is $J_{\text{silicene}} = 1.14eV$, see SchÃ¼ler et al. [20].

In this simulation time is measured in units of t_0, with

$$t_0 = \frac{\hbar}{J} = 6.58212 \cdot 10^{-16} s. \tag{3.2}$$

As seen in section 2.2.1, for the non interacting case the kinetic energy of the electrons has the magnitude of J. Thus, considering the TDSE, t_0 is a good choice for the time unit, because the dynamics are expected to happen on this timescale. The lattice parameter a_0 is chosen to be $a_0 = 1.42\text{Å}$, which is the lattice parameter for graphene. The charge q is chosen in a way that

$$W_0 = -\frac{eq}{4\pi\epsilon_0 a_0} = 50eV. \tag{3.3}$$

While this, too, is not chosen to describe any specific setup, the interaction is of the correct magnitude, as for example for $q = 2e$ and $a_0 = 1.42\text{Å}$ one would

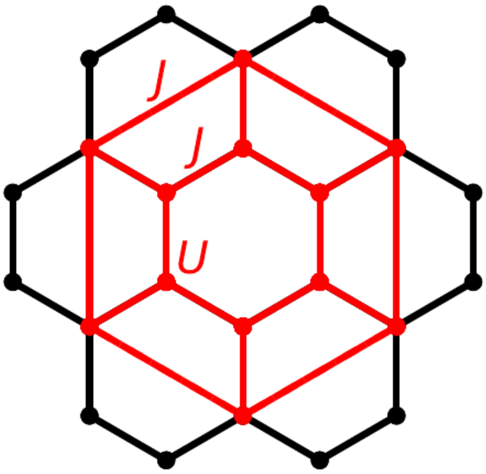

Figure 3.1: A 24 site lattice with the used 12 site system highlighted in red. The red lines between lattice sites represent the possibility of hopping between those sites with the hopping constant J. The on-site interaction is U.

get $28.8eV$. The projectile is initially moving along the z-axis: $\vec{v_0} = v_0\vec{e_z}$. The lattice lies in the plane at $z = 0$. The projectile has a fixed starting distance of $z_p(t = 0) = 100$Å from the lattice. At this distance, the field of the electrons is very much screened by the atomic cores, because the distance is a lot bigger than the extent of the lattice, which is only a few , $d_{\text{lattice}} \leq 5$.

While the duration of each simulation depends on the projectile velocity, the duration is always chosen in a way that the projectile, which has started at $z_p(t = 0)$, penetrates the lattice at around 40% of the simulation time. Thus the system has enough time to evolve after the projectile has passed, which enables the examination of stable changes to the lattice induced by the projectile.

3.1 Honeycomb Lattice

Considering two dimensional lattice types, the honeycomb lattice is particularly interesting because real materials like graphene, magnesium ([7]) or pnictogens ([14]) have this structure. Therefore, the studies of particle induced doublons in this thesis have been done on honeycomb-structured lattices.
To make the simulation via exact propagation possible when using the Hubbard Hamiltonian, the system has to be small in order to minimize the number of basis states. For this thesis, a symmetric lattice is chosen to retain the symmetries of the honeycomb lattice.

Because a 24 site setup , see 3.1, could not be treated with the available computational resources, the simulations are done on a reduced honeycomb lattice. This lattice consists of 12 sites. For 12 sites at half-filling with 6 ↑-electrons and 6 ↓-electrons the number of basis states becomes $\binom{12}{6} \cdot \binom{12}{6} = 853776$, which is a large number, but the Hamiltonian can still be diagonalized using the Lanczos method. For 24 sites at half-filling with 6 ↑-electrons and 6 ↓-electrons, there would already be more than $7 \cdot 10^{12}$ basis states. When just cutting out 12 sites of the 24-site lattice, the six outer sites only have one nearest neighbour each. With

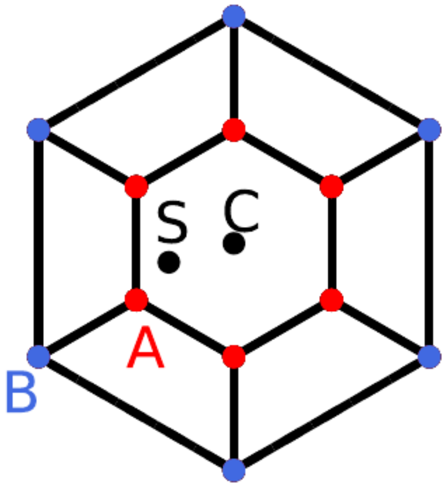

Figure 3.2: The reduced honeycomb lattice with the sites A and B highlighted, which represent all red and blue sites. The starting positions C and S are projected into the lattice plane

the Hubbard Hamiltonian highly depending on the number of nearest neighbours each site has, just using the 12 sites would not represent the honeycomb lattice accurately. Therefore, hopping is considered to be possible between two neighbored outer sites, with the same hopping constant t as for nearest neighbors, see3.1. With this change to the lattice model, the number of nearest neighbors is the same as for the honeycomb lattice of infinite size as far as the Hubbard Hamiltonian is concerned. The only difference is now the lattice symmetry. Symmetry based deviations, however, are expected to occur for any small sized finite systems. This way of reducing the honeycomb system is preferred over alternatives such as periodic boundary conditions. These would, for example, connect the outer sites to those on the opposite edges of the lattice, but the possibility of hopping between these sites would be even lower in a real lattice and the symmetry would be changed as well.

The projectile penetrates the lattice at $z = 0$. The starting position of the projectile is first chosen to be $C = (0, 0, 100\text{Å})$, far above the center of the 12-site system as shown in 3.1. To examine the influence of the initial projectile position on the results, this position is later changed to $S = (\frac{\sqrt{3}}{3}a_0, -\frac{1}{6}a_0, 0)$, which was predicted to be the passing location with the most average behaviour by DFFT calculations for graphene ([27]) , which has the honeycomb structure discussed here. When considering the projectile position C, the symmetry of the setup ensures that at any given time the lattice properties of the sites are only dependent on their distance to C. Thus the full system information is accessible when only looking at sites A and B. This simplifies the discussion of the results for the densities and double occupation, because the graphs for just two sites have to be discussed.

Chapter 4

Results and analysis

When the projectile passes through the lattice, the force it creates on the lattice electrons prompts them to move towards it. After the projectile has passed, the projectile has a lower kinetic energy than before. This energy was transferred to the lattice. One cause of this energy loss is the creation of stable doublons in the lattice.

In this chapter, the results of the simulations done for this thesis are shown and discussed. First the dynamics happening, that lead to the production of doublons on the lattice, are presented and discussed. Secondly the doublon production is analyzed by varying projectile velocity, interaction strength and the initial projectile position. The correlation of the increase in double occupancy and stopping of the projectile is examined. Finally a simplified to two-site model is introduced to get a better understanding of the doublon production induced by the projectile. The Landau-Zener effect is used as an approach to describe the important transitions on this two site model.

4.1 Dynamics

The energy transfer and the dynamics happening on the lattice can be analyzed by looking at the evolution of the density and the double occupation. For a starting velocity $v_0 = 5\text{Å}/t_0$ the time dependent density, double occupation and projectile energy are shown in this section. The penetration point is C. Thus, only the two lattice sites A and B are considered, see chapter 3.

As for the density $n_i = \langle \hat{n}_i \rangle_\Psi$, it can be seen that the starting value is $n_i = 1$ for all U for both sites. This is due to the symmetry of the Hamiltonian when the field of the projectile is not present. Every site has three nearest neighbours with the hopping amplitude J and the same on-site interaction strength U.

When the projectile approaches the lattice closely, the induced force on the electrons makes them shift towards site A. This results in the density on site A increasing, and thus decreasing at site B, due to conservation of the total particle number: $n_B = 1 - n_A$. Right after the projectile passes the lattice at $t \sim 20t_0$, the density on site A reaches its maximum value.

When looking at this maximum value for the density, no simple dependency on the interaction strength can be observed. The maximum density on site A is

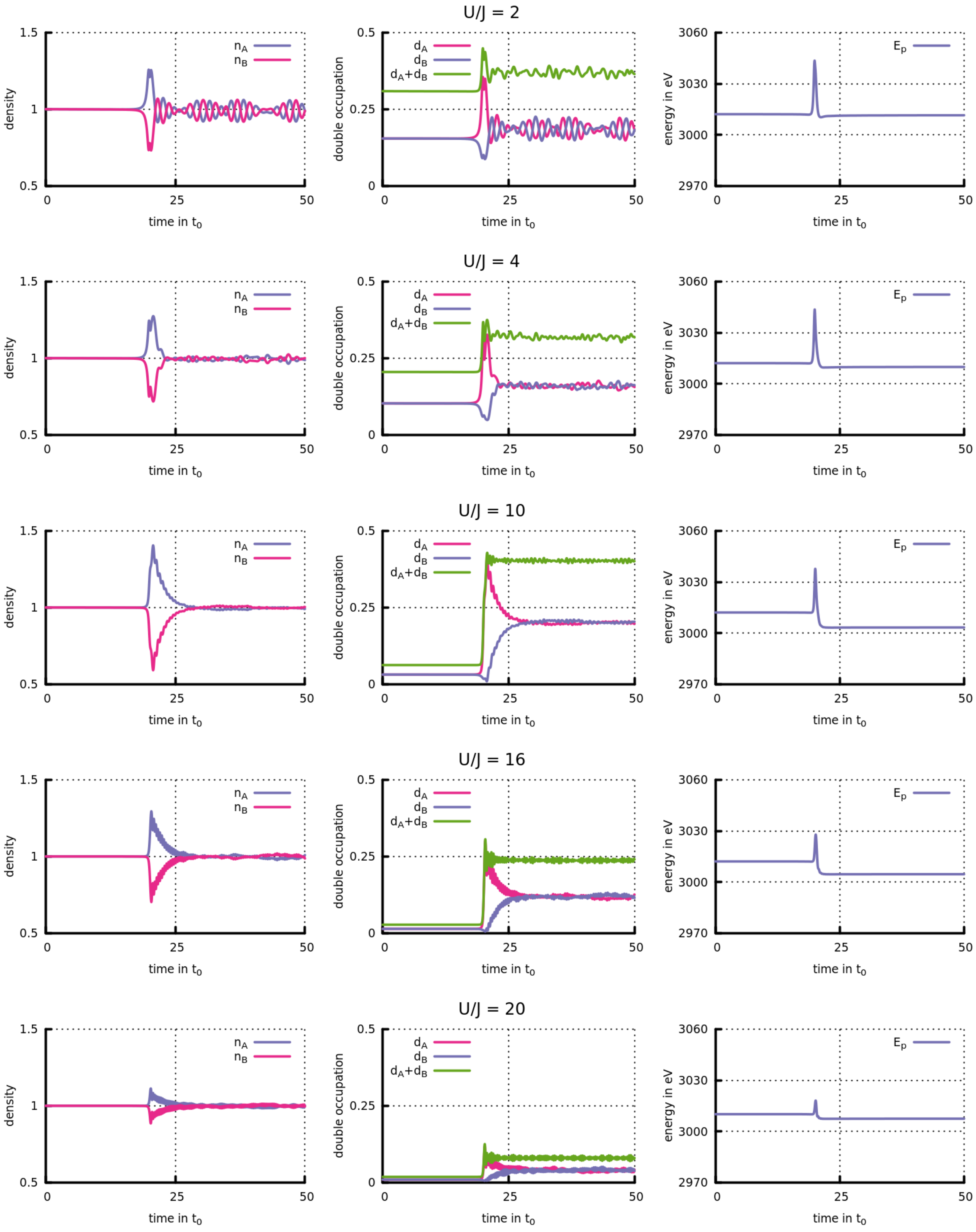

Figure 4.1: Time evolution of density, double occupation on sites A and B and projectile energy for the starting velocity $v_0 = 5\text{Å}/t_0$ and the initial projectile position $C = (0, 0, 100\text{Å})$ for $U/J = 2, 4, 6, 10, 16, 20$. Results for $U/J = 0$ are not presented due to significant deviations compared to the results obtained by Balzer [2]

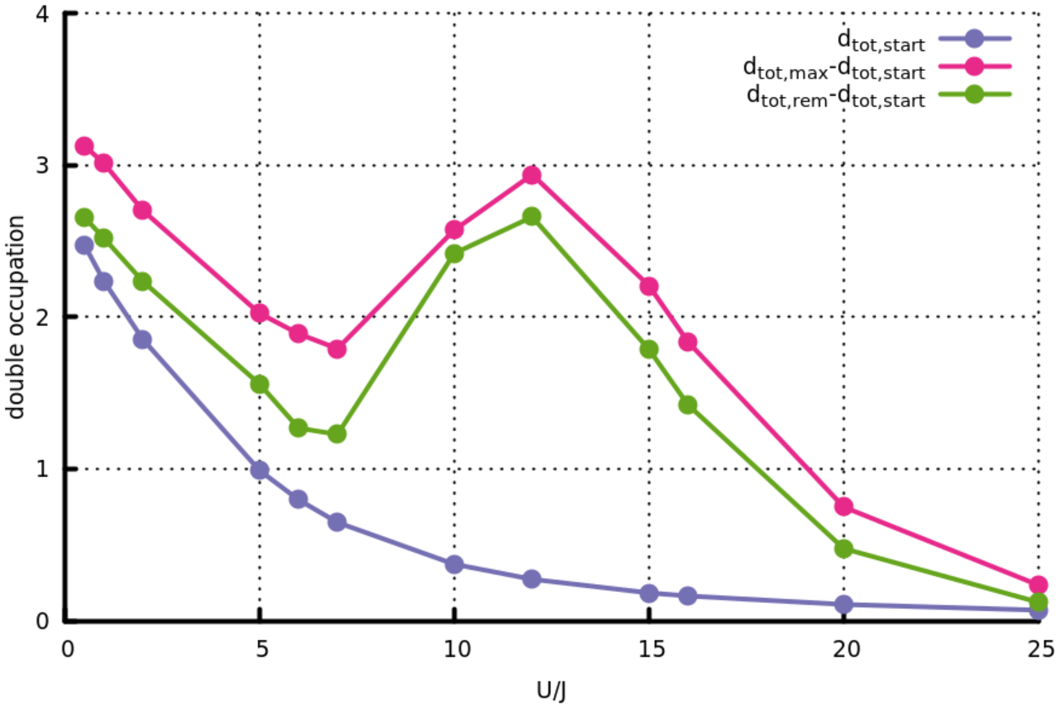

Figure 4.2: Starting values $d_{tot,start}$ for simulated U/J. Difference of remaining total double occupation $d_{tot,rem}$ and maximum total double occupation $d_{tot,max}$ to its starting value for various U/J at $v_0 = 5\text{Å}/t_0$.

higher for $U/J = 10$ than for the higher and lower interaction strengths presented. It seems to have a maximum for a certain U/J for this projectile velocity.

With the projectile moving away from the lattice plane, for times $> 20t_0$ the density at site A decreases again. The speed of this motion seems to be lower the larger U/J. At the end of the simulation, the n_A- and n_B-values oscillate around the starting value. In absence of the projectile potential, the electrons again spread over the lattice. The observed oscillation is very likely due to the finite size of the lattice and the high symmetry of the system. In a larger system, the density could dissipate further after the passing of the projectile, which would lead to a lower oscillation amplitude. For a lattice of infinite size, no oscillations are expected. The oscillation amplitudes are in general larger for smaller U/J, which can be explained by weaker damping through the onsite repulsion, that blocks the oscillations, when the site is occupied.

The starting values of the double occupation depend on the choice of the interaction strength. This is because, with increasing U/J, the ground state, which is the eigenstate with the lowest energy, needs to have lower double occupation. For various U/J this dependency can be seen in fig. **??** for the total double occupancy which in this setup due to the symmetry is simply: $d_{\text{tot}} = 6 \cdot (d_A + d_B)$

When the projectile comes closer to the lattice and the electrons move to site A, the double occupation on site A increases and decreases at site B, as would be

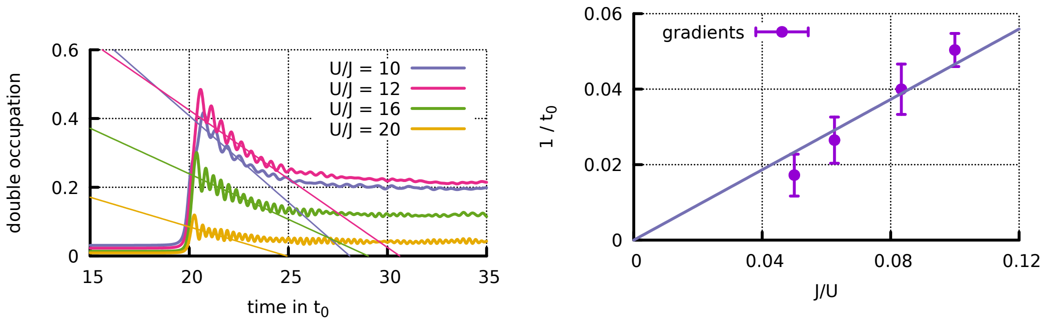

(4.3.1) time evolution on site A for different U/J and $v_0 = 5\text{Å}/t_0$

(4.3.2) gradients of the doublon dissipation from site A the linear regressions over the inverse relative interaction strength

Figure 4.3: linear regression for the dissipation of the double occupation on site A

expected. The maximum of the double occupation on site A correlates with the maximum of the density, as expected. The same dependency on the interaction strength is observed.

While the sum of densities on sites A and B is constant, for the double occupation $d_A(t) + d_B(t)$ this is not true. When the projectile passes the lattice, the total double occupation increases and reaches its maximum value right after the projectile penetrates the lattice, at the same time as the double occupation on site A is maximal. This built up double occupation, however, does not completely vanish again for $U/J > 0$. For $U > 0$ the increase in double occupation leads to an increase in lattice energy that cannot be dissipated on the finite size system. For $U > J$ the thoughts in 2.2.2 also predict a conservation of double occupation. Therefore, the particle induced double occupation can be interpreted as the creation of doublons on site A. The total double occupation is the most important quantity to measure the appearance of doublons, even when dislocated over the lattice sites.

When the distance of the projectile increases, the total double occupation decreases. For late times, if $U > 0$, the double occupation on all sites approaches some value higher than the initial one, because the doublon governed by the Hamiltonian in 2.29 is then fully dislocated on the system. As for the dissipation time, it can be seen very clearly that the dissipation of the double occupation over the lattice is slower the larger U/J. For low U/J the dissipation is hard to analyze due to the short timescale and the oscillations. For some large U/J the the dissipation speed is analyzed and shown in fig. 4.3. A linear regression is done for the dissipation of the double occupation on site A, where the doublon is created. The gradients of the regression function are plotted over the inverse relative interaction strength J/U. The error bars are due to the regression errors. The plot shows a good agreement with the theory of 2.2.2, which predicts the propagation time of the doublons to be proportional to the inverse interaction strength, because the effective hopping constant is ([17]).

In the last graph, the projectile energy during the simulation is shown for each U/J. Its initial value is the same for all U/J, because the same starting velocity is considered. Neglecting any interaction with the lattice at the distance of 100Å, the initial projectile energy becomes:

$$E_p(0) = \frac{1}{2} m_p \vec{v}_0^2 = 3.0121 keV. \tag{4.1}$$

When the projectile is moving close to the lattice, its energy increases. The lattice electrons move towards the inner sites, while the positively charged atomic cores do not change their position. This results in the projectile being accelerated. When moving away, the the projectile gets slowed down and thus its energy decreases. At a far distance from the lattice, when the projectile is barely interacting with it, its energy is lower than initially. This energy difference is called stopping power:

$$S_p = E_p(t_{max}) - E_p(0), \tag{4.2}$$

where $E_p(t)$ is the projectile energy and t_{max} is the maximum time of the simulation. This energy loss can be explained with the delayed reaction of the lattice electrons, which results in the projectile being slowed down more when moving away by the electrons that are already on site A, than accelerated when moving towards the lattice. For the considered projectile velocities, the stopping power is small compared to the initial projectile energy. Thus the projectile is approximately moving at a constant speed, except for when passing the lattice.

Because of energy conservation, the stopping power also measures the energy transferred to the lattice. For $U/J > 0$, one reason for the increased lattice energy is a larger double occupation. The correlation between stopping power and the remaining double occupation is discussed **??** in the next section.

4.2 Analysis of the doublon production

When observing doublon production, the most interesting quantity is the total double occupation on the lattice, mainly the difference of the remaining value d_{rem} after the projectile is gone and the initial one d_{start}, which is a measurement of the stable increase in double occupation due to doublons. The remaining double occupation is calculated by averaging over the total double occupation for $t > 0.7t_{max}$. During this time, the double occupation has been observed to be stable, or at least oscillating around a certain value, for all simulations done. Because the oscillations are highly stable and symmetric after $t = 0.7t_{max}$, the computed relative errors of this averaging are in any case (except for U=0, which is not treated) smaller than 1%.

To take into account the impact of the initial projectile position on the doublon production, the results for the two different initial projectile positions S and C are compared, see sec 3.

The results for C that are used in this section have been obtained by Balzer [2]. The main difference to the other simulation results presented in this thesis is the projectile velocity being constant. This means that the retroactive effect of the lattice on the projectile is neglected. Thus the projectile does not get slowed down or accelerated and moves with the constant velocity v_0, this corresponds to an infinite projectile mass. This should not make a huge difference when considering most projectile velocities simulated, because of the high projectile energies. As seen in the previous section for $v_0 = 5\text{Å}/t_0$, the projectile energy is of a much larger magnitude than the changes induced by the lattice, which leads to the velocity barely changing. For low velocities however the energy transfer to the lattice might be of the magnitude of the kinetic energy. For $v_0 = 0.5\text{Å}/t_0$, for example, the initial projectile energy is only around $30eV$.

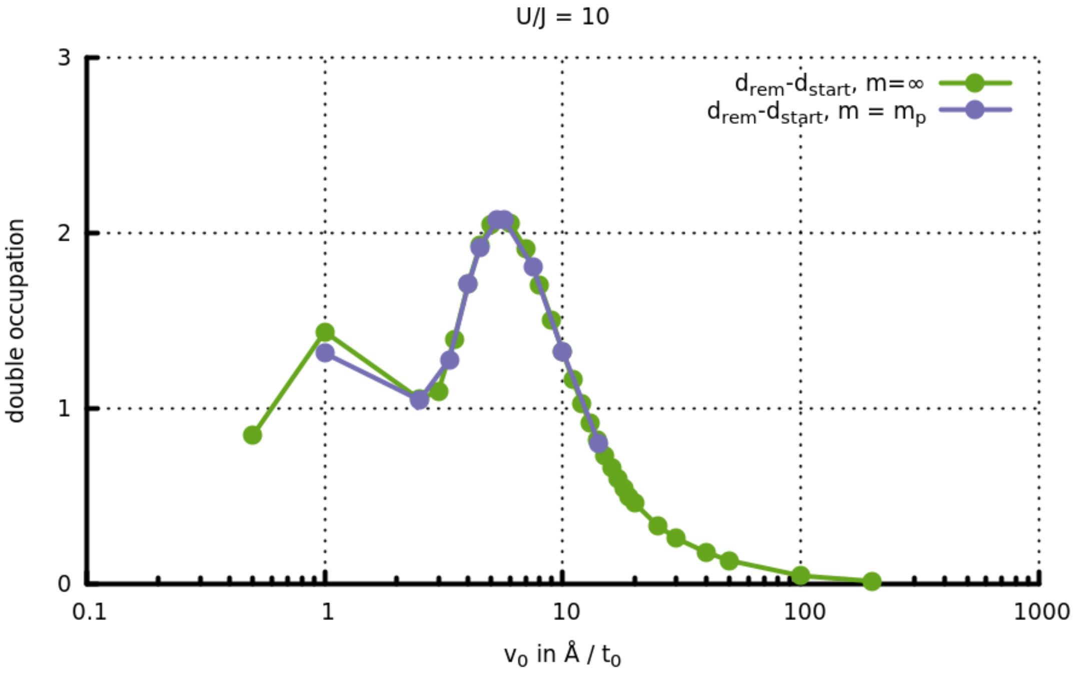

Figure 4.4: Difference of remaining total double occupation and double occupation at $t = 0$ for various v_0 at $U/J = 10$.

To evaluate the impact of this difference, simulations calculated by Balzer [2] have been reproduced with the projectile mass $m = m_p$ for various U/J and v_0. The comparison shown in fig 4.4 for $U/J = 10$ generally indicates a very good agreement. For low projectile velocities, however, the differences in the results increase.

For $v_0 < 1$ the agreement would not expected to be as good, because of the kinetic projectile energy being of the same magnitude as the stopping power. For higher velocities, the results from Balzer [2] can, however, be compared to those obtained for the initial projectile position S using $m = m_p$.

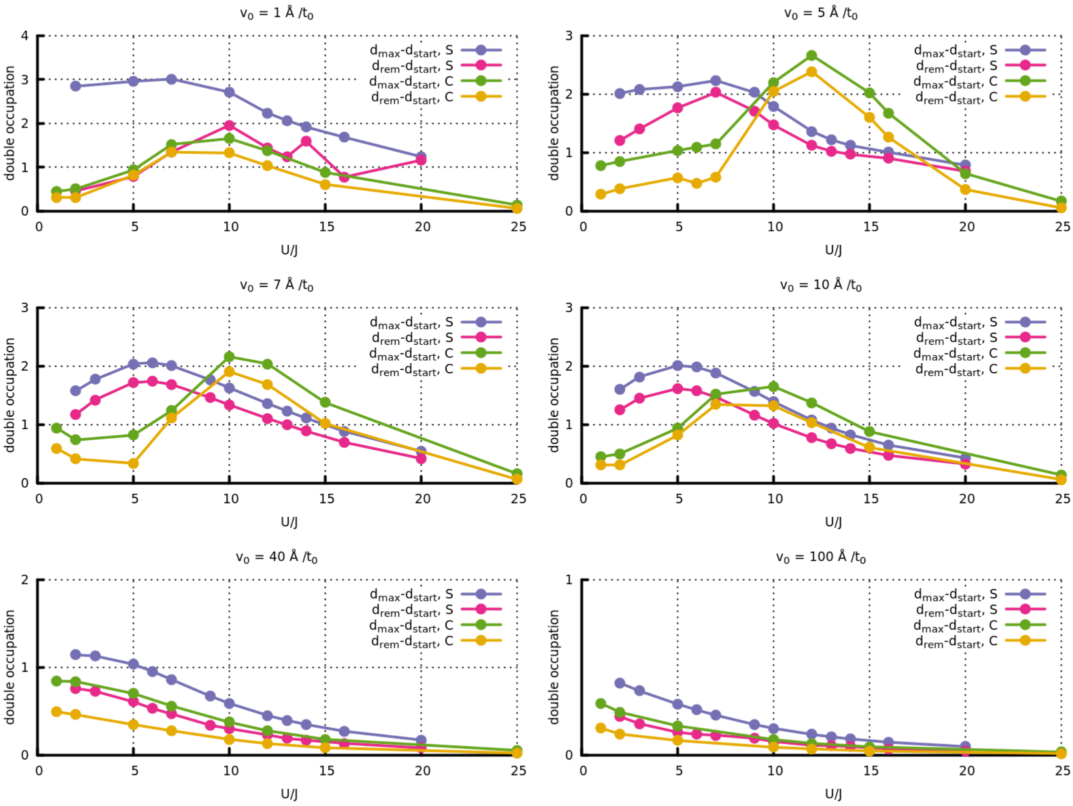

Figure 4.5: Increase in double occupation after the projectile has passed and at its maximum over U/J. Different projectile velocities are considered from $v_0 = 1\text{Å}/t_0$ to $v_0 = 100\text{Å}/t_0$.

4.2.1 Dependency on U/J

As seen in section 4.1, the production of doublons strongly depends on the interaction strength of the system. For $U/J = 0$, no doublons can form. The larger U/J, the greater the stability of created doublons. But for highly correlated systems the forming of doublons drastically increases the lattice energy. In the limit of large U/J, the double occupation thus cannot increase due to the projectile interaction. Therefore, the double double occupation is expected to have a maximum value for some finite interaction strength. This can be seen in fig 4.5. The exact position of this maximum seems to be dependent on the projectile velocity and on the initial position of the projectile. The dependence on the initial projectile position suggests the doublon production to be highly dependent on the symmetry of the whole setup. This is substantiated by the connection of remaining and maximum double occupation on the lattice, as those quantities correlate even for relatively small interaction strengths. This correlation also implies the doublons to be stable for relatively small U/J, leading to the assumption that the remaining double occupation for $U/J \geq 2$ directly depends on the dynamics occurring right after the projectile penetrates the lattice.

For high projectile velocities, the position of the maximum in doublon production shifts towards smaller interaction strengths. This can be explained by the short reaction time of the lattice electrons at high projectile velocities and the increasing on-site repulsion for electrons on one site, which hinders the electrons in creating doublons on the sites closest to the projectile.

4.2.2 Dependency on v_0

To understand the dependence on the projectile velocity, it is best to consider the limiting cases. For a very low projectile velocity, the reaction time of the system increases more and more. If the projectile mass is considered to be infinite, the system behaves adiabatically in the limit for low v_0, which means that it is always in equilibrium due to the long reaction time. In this case the process is completely time reversible. Therefore, the system has to remaining the groundstate at the end of the simulation.

For a finite projectile mass, the limiting case for low velocity would be the projectile simply moving towards the lattice, but not passing it. However, in all simulations presented in this thesis, the projectile velocity was sufficiently high to pass the lattice and never be fully stopped. Therefore, this limiting case does not need to be considered. Nevertheless, lower energy transfer to the lattice is expected to happen in both cases, due to the more adiabatic behaviour of the system.

For very high projectile velocities, the reaction time of the lattice electrons is very short. In the limiting case, no double occupation could be built up. The system would stay in the same state, because there would be no time to react to the changing Hamiltonian.

This leads to the expectation for the doublon production to have a maximum regarding a changing projectile velocity, as was the case regarding changing U/J. As can be seen in fig. **??**, the doublon production for high v_0 behaves as expected. For the projectile position S the doublon production lowers for small projectile velocities, leaving a single maximum. For C, other maximums can be seen. The largest maximum is the one at the highest v_0. The comparison of the results for C and S, leads to the assumption that the other maxima are due the high symmetry of the setup with regard to the initial projectile position C. The behaviour is reminiscent of oscillations, which could be caused by the many different symmetries of this setup. For the projectile position S, these other maxima are not observed.

The general character of the dependency on U/J seems to be highly dependent on the specific system symmetry, although the trends for very low and high v_0 imply the existence of at least one maximum, which is, in all considered cases, situated at smaller velocities.

4.2.3 Maximum doublon production

Motivated by the existence of maxima looking individually at interaction strength as well as projectile velocity, now the existence of a maximum with regard to

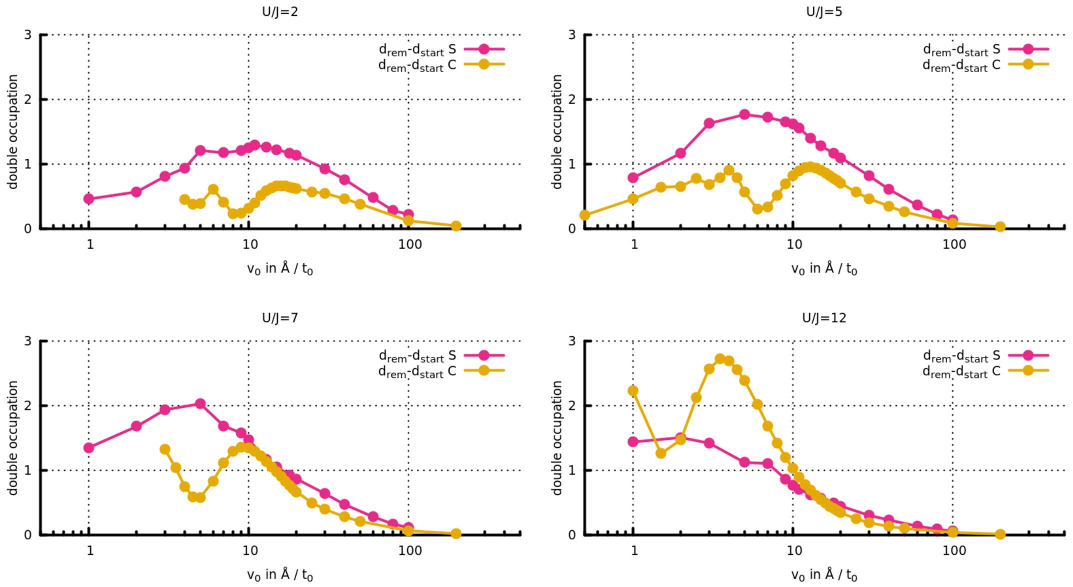

Figure 4.6: Dependency of the doublon production on the projectile velocity for the two initial projectile positions C and S and relative interaction strengths $U/J = 2, 5, 7, 12$. For the projectile velocity a logarithmic scale is used. The results for the projectile position C where obtained by Balzer [2]

both parameters is inspected. Figure 4.7 and figure 4.8 show surface-plots for the remaining double occupation, dependent on the relative interaction strength and the initial projectile velocity. The expected maximum can be clearly seen in both setups. However, its exact position differs from the expectation formed in the previous analysis. For S, the maximum is at $U/J = 9(+1, -2)$, $v_0 = 3(\pm1)\text{Å}/t_0$ with $d_{\text{rem}} - d_{\text{start}} = 2.13$. For C, it can be found at $U/J = 15 \pm 3$, $v_0 = 3 \pm 1\text{Å}/t_0$ with $\text{rem} - d_{\text{start}} = 2.77$. The uncertainties for the positions of the maxima are due the resolution of the grid used to scan the parameters U/J and v_0. Although the interaction strengths of the maxima for C and S as well as their extent differ significantly, this result allows to somewhat specify the intervals where large doublon production is expected for this setup: $U/J \in [7, .., 20]$ and $v_0 in\text{Å}/t_0 \in [2, ..., 10]$. The maximum increase in double occupation is 2.13 or 2.77, which for the 12 site system would mean an increase in double occupation of 0.18 or 0.23.

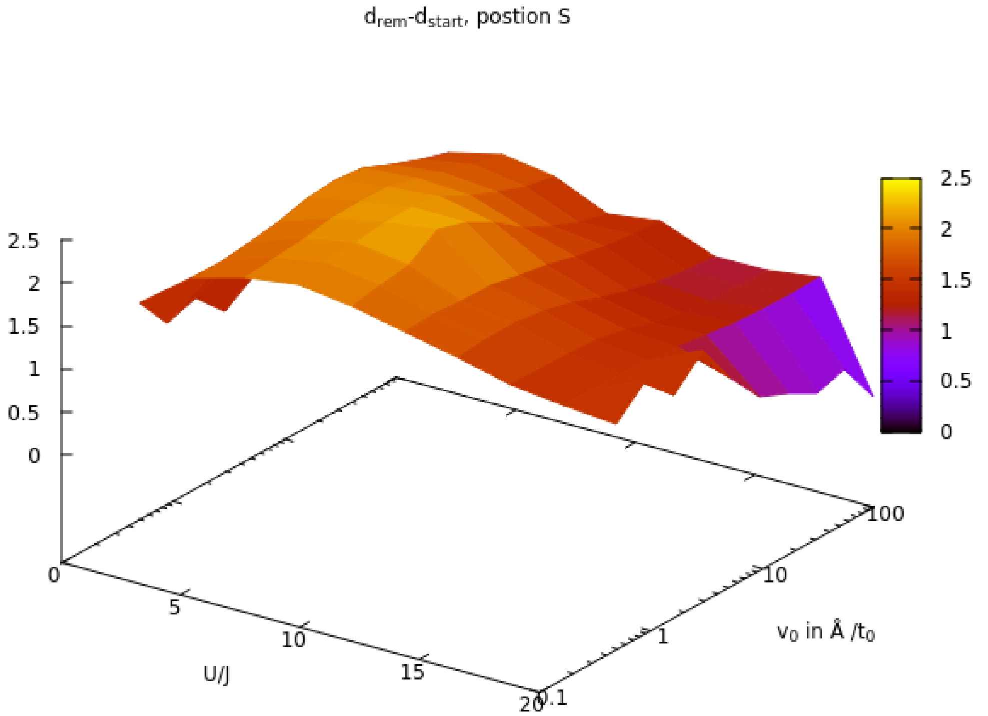

Figure 4.7: The remaining increase in double occupation on the lattice dependent on U/J and v_0 for all simulated parameters and the initial projectile position S . The interpolation for this plot was done with gnuplot. The maximum is at $U/J = 9$ and $v_0 = 3\text{Å}/t_0$, with $d_{\text{rem}} - d_{[}\text{start}] = 2.13$

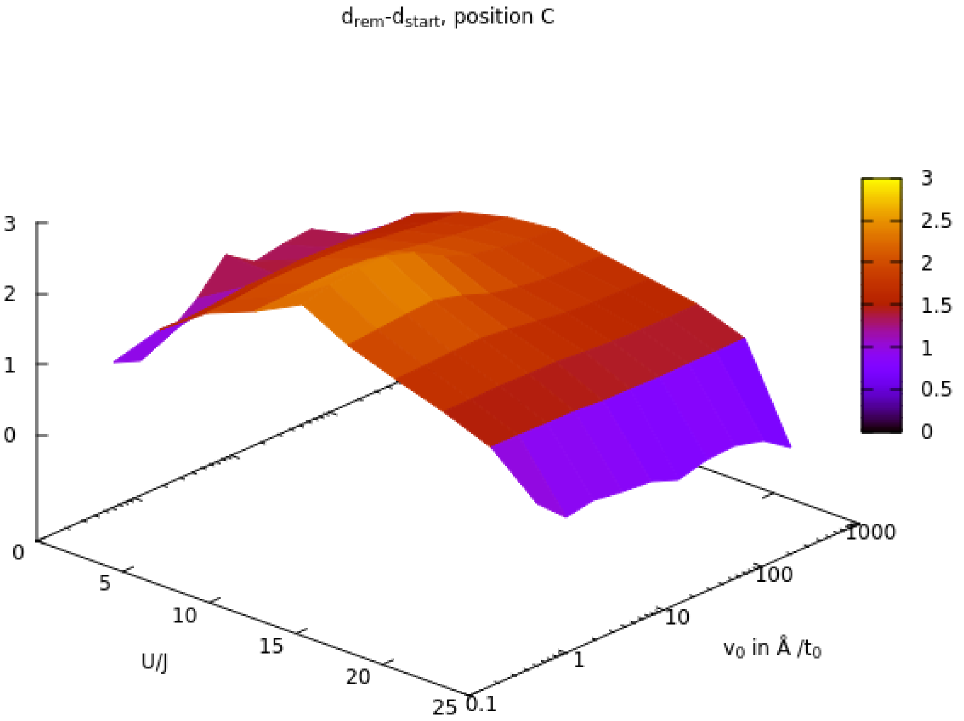

Figure 4.8: Surface-plot for the remaining increase in double occupation on the lattice dependent on U/J and v_0 for all simulated parameters and the initial projectile position C, generated from the results obtained by Balzer [2]. Interpolation for this plot was done using gnuplot. The maximum is at $U/J = 15$ and $v_0 = 3\text{Å}/t_0$, with $d_{\text{rem}} - d_{[}\text{start}] = 2.77$

4.3 Doublon creation and stopping power

Another interesting aspect is the stopping effect that the doublon production has on the projectile. The energy increase of the lattice due the increase in double occupation can be calculated by:

$$E_{\mathrm{d}} = (d_{\mathrm{rem}} - d_{\mathrm{start}}) \tag{4.3}$$

In figure 4.9, this energy is compared to the stopping power for various U/J, using initial projectile position S, although the same correlation behaviour is observed for C. Comparison shows that the correlation of stopping power drastically increases the higher U/J. While the doublon production has close to no influence for $U/J = 2$, at $U/J = 5$ around half of the energy transferred to the lattice is stored in doublons. For $U/J \geq 12$, the effect of doublon creation completely dominates the stopping of the particle. This interrelation of doublon production and stopping power is very plausible, considering that the energy per doublon linearly increases, whereas the possibility of energy dissipation lowers with increasing U/J. The strong correlation of doublon creation and stopping power also marks the importance of the studied effect when describing highly correlated systems. However, to accurately evaluate its influence in stopping an ion at a realistic surface, models including other energy dissipation possibilities, like ionization effects and phonons, would be needed.

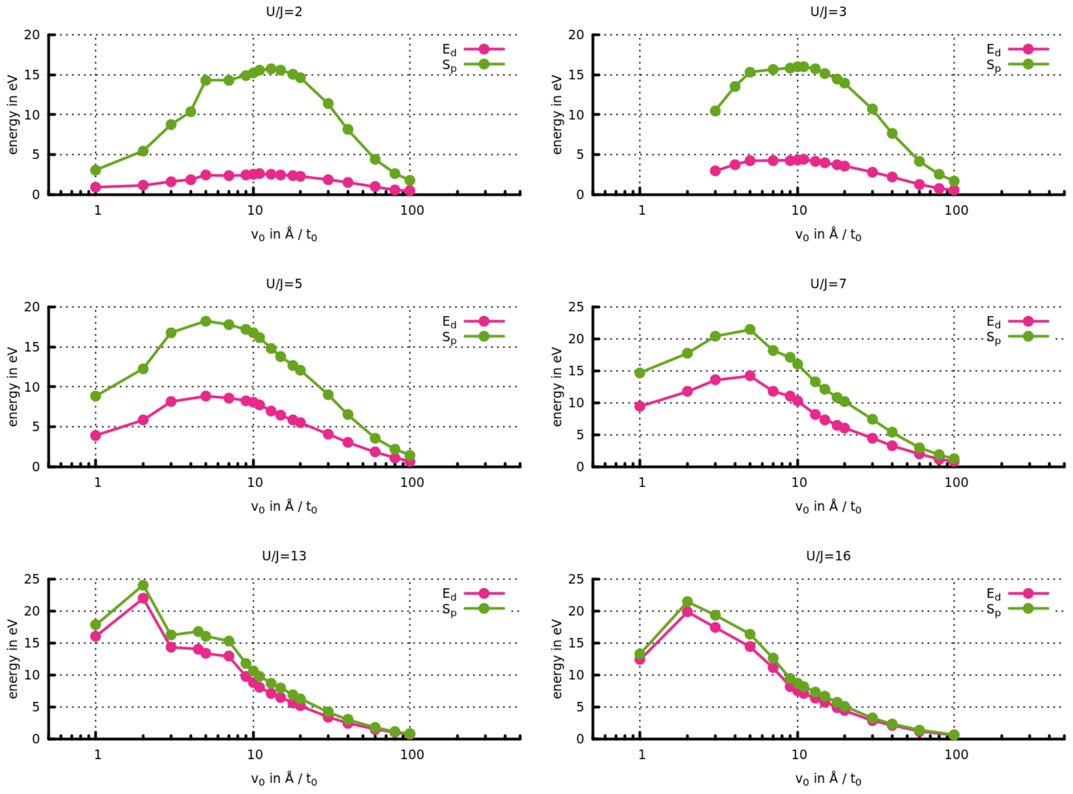

Figure 4.9: Energy increase due to double occupation E_d and stopping power S over the projectile velocity, for $U/J = 2, 3, 5, 7, 13, 16$

4.4 Two-site setup

To better understand the doublon production in the projectile setup, a relatively simple setup is considered: A two site setup. The setup is presented in 4.10. It consists of two lattice sites at $r_1 = (0, 0, 0)$ and $r_2 = (a_0, 0, 0)$ with $a_0 = 1.42$. The starting position of the projectile is $r_p(0) = (2a_0, 0, 100\text{Å})$. Due to the high projectile velocities considered, the projectile can be assumed to move nearly parallel to the z axes. For this projectile velocity and interaction strength the projectile moves less than 0.02Å away from $x = 2a_0$. Due to the symmetry of the honeycomb setup when considering the projectile position C, its dynamics are expected to be similar to those of the two site setup. In fig. 4.11 the time

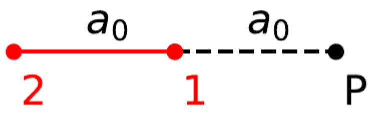

Figure 4.10: The two site setup with the lattice highlighted in red, consisting of the sites 1 and 2 with the initial position of the projectile P projected into the lattice plane

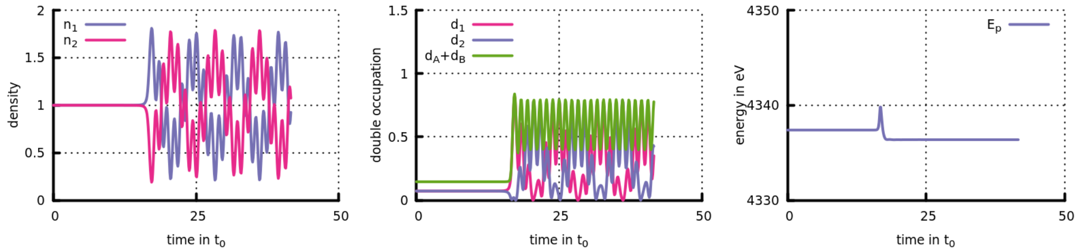

Figure 4.11: Density and double occupation of the two site setup for $V_0 = 5\text{Å}/t_0$ and $U/J = 4$

dependent density and double occupation observed when simulating the two-site setup are shown exemplary for $v_0 = 6\text{Å}/t_0$ and $U/J = 4$. Although the results are quantitatively different from those of 4.1, qualitatively they are very similar. The electron density on site 1 increases as the projectile comes closer and a higher double occupation is build up. When the projectile is moving away, the double occupation spreads out over the lattice sites, but the total double occupation stays at a higher level than initially. This indicates that doublon production can be observed studying this model. Although this being is a far less realistic setup, the main advantage of this model is its simplicity. The Hamiltonian for this system is the Hamiltonian for the dimer with an additional term for the projectile interaction:

$$\hat{H}(t) = -J \sum_{\langle i,j \rangle, \alpha} \hat{c}^{\dagger}_{i\alpha} \hat{c}_{j\alpha} + U \sum_i \hat{n}_{i\uparrow} \hat{n}_{i\downarrow} + \sum_i W_{ii}(t) \left(\hat{n}_{i\uparrow} + \hat{n}_{i\downarrow} \right) \tag{4.4}$$

Using the basis of 2.2.3 for half filling the Hamiltonian in matrix form becomes:

$$H = \begin{pmatrix} W_{11} + W_{22} & 0 & -J & -J \\ 0 & W_{11} + W_{22} & J & J \\ -J & J & U + 2W_{11} & 0 \\ -J & J & 0 & U + 2W_{22} \end{pmatrix} \tag{4.5}$$

This matrix can be diagonalized analytically. For a projectile moving parallel to the z-axis, the eigenvalues of this Hamiltonian for $U/J = 4$ can be seen in fig. 4.12. At a large projectile distance those eigenvalues converge towards the dimer eigenvalues calculated in 2.2.3. However with the projectile close to the lattice the eigenenergies drastically change. All eigenenergies lower due to the negative interaction potential. The projectile breaks the symmetry between sites 1 and 2. The eigenstates also change, which can be seen for example when looking at their double occupation, see fig. 4.13. As can be seen in fig. 4.12 the perturbation induced by the projectile prompts E^U to overcome the Hubbard gap.

For doublons to be created in the process it is necessary that for large t the states $\left|\Psi^U\right\rangle$ and $\left|\Psi^+\right\rangle$ are occupied. Therefore at some point a transition into one of those states has to happen.

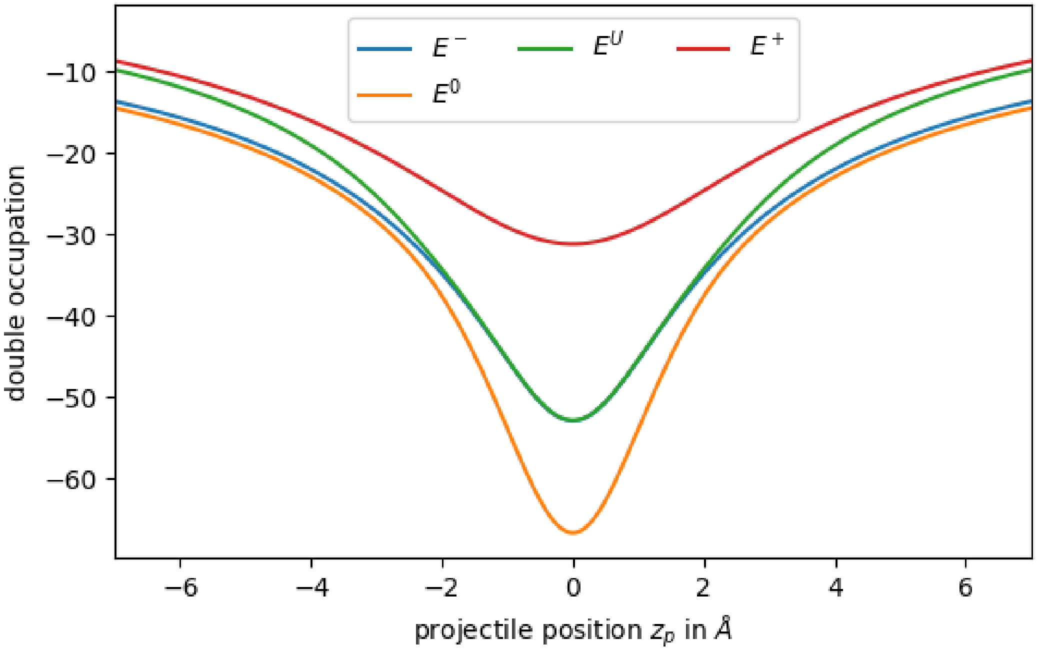

Figure 4.12: Eigenvalues of the Hubbard dimer depending on the projectile position on the z-axis. Using $U/J = 4$

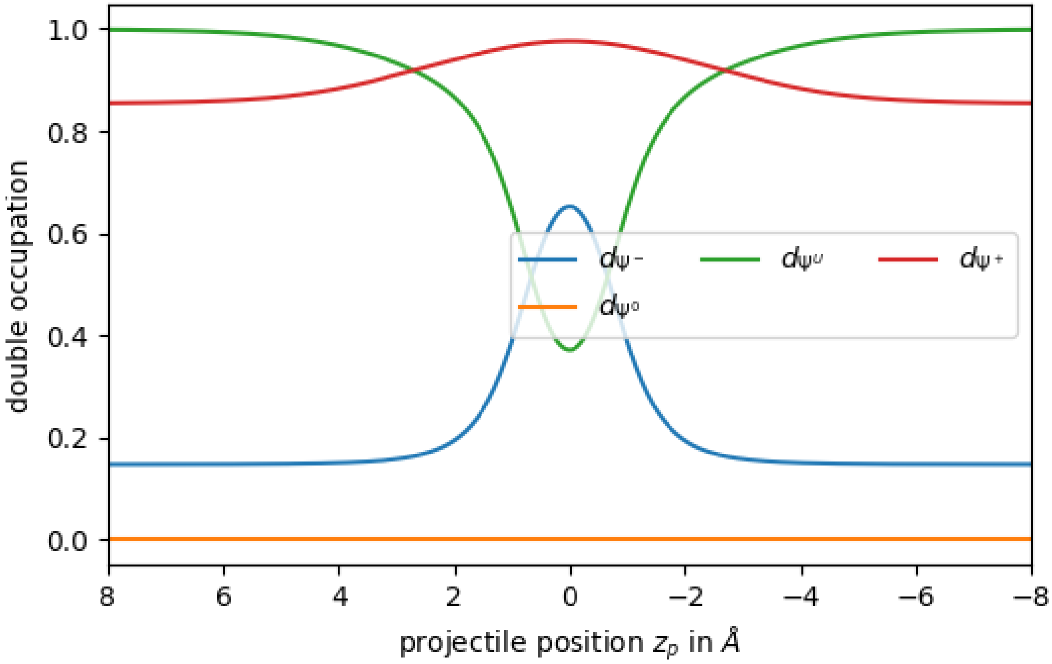

Figure 4.13: double occupation of the eigenstates for $U/J = 4$ depending on the projectile position z_p

Figure 4.14 shows the full time dependent energy spectrum of the two-site setup for $U/J = 4$ and $v(0) = 6/t_0$. This is available due to the low number of basis states of the system. The pixelated and broadened spectrum is due to the resolution when saving and plotting the spectrum, which in reality consists of delta-functions. The system behaves as one would predict from just looking at its eigenvalues. Fist an excitation into $\left|\Psi^U\right\rangle$ is observed. Later a crossing into $|\Psi^+\rangle$ is happening, when the eigenvalues E^U and E^+ approach again.

However no excitation from the groundstate into $|\Psi^0\rangle$ is observed. If treating the whole setup with perturbation theory, although the perturbation by the projectile is not small, this crossing is expected to be forbidden due to its matrix element V_{-0} being zero:

$$\begin{aligned}
V_{-0} &= \left\langle\Psi^-\right| \left(W_{11}\left(n_{1\uparrow}+n_{1\downarrow}\right)+W_{22}\left(n_{2\uparrow}+n_{2\downarrow}\right)\right)\left|\Psi^0\right\rangle \\
&= \left\langle\Psi^-\right| \left(W_{11}\left(n_{1\uparrow}+n_{1\downarrow}\right)+W_{22}\left(n_{2\uparrow}+n_{2\downarrow}\right)\right)\frac{|\Psi_1\rangle+|\Psi_2\rangle}{\sqrt{2}} \\
&= \frac{\left(\langle\Psi_2|-\langle\Psi_1|\right)+\frac{E^+}{2J}\left(\langle\Psi_3|-\langle\Psi_4|\right)}{\sqrt{2+\left(\frac{E^+}{\sqrt{2}J}\right)^2}}\,\frac{(W_{11}+W_{22})(|\Psi_1\rangle+|\Psi_2\rangle)}{\sqrt{2}} \\
&= \frac{(W_{11}+W_{22})-(W_{11}+W_{22})}{\sqrt{4+\left(\frac{2E^+}{\sqrt{2}J}\right)^2}} \qquad (4.6) \\
&= 0 \qquad (4.7)
\end{aligned}$$

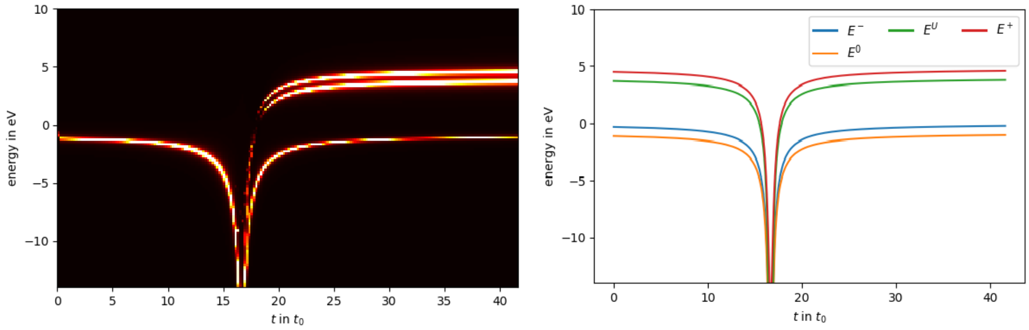

Figure 4.14: The time dependent energy spectrum for $U/J = 4$ and $v_0 = 6\text{Å}/t_0$ and the time dependent exact eigenvalues of the system for $U/J = 4$ and $v_0 = 6\text{Å}/t_0$. The eigenvalues are computed by using the time dependent projectile position to calculate the interaction

When looking at the time dependent spectrum, one can see the transitions, occur at the time of the difference of respective eigenvalues being minimal. For the first transition from $|\Psi^-\rangle$ to $\left|\Psi^U\right\rangle$ this is illustrated in fig. 4.15

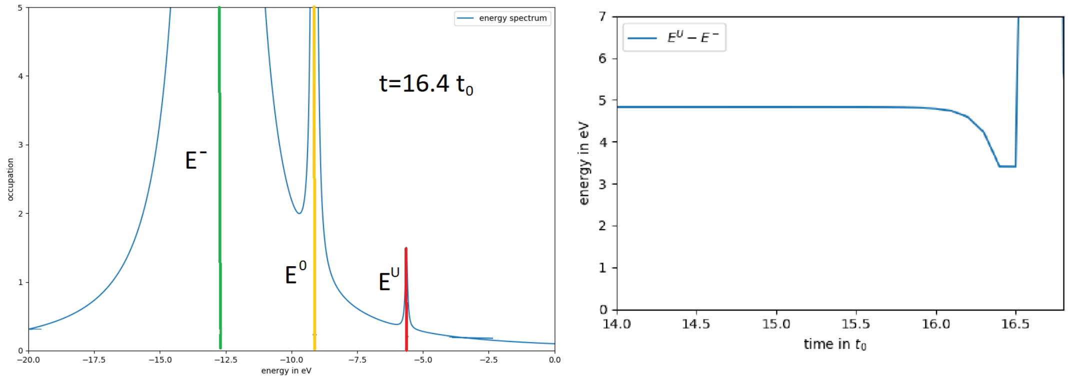

Figure 4.15: The time dependent difference of energy eigenvalues E^U and E^- with the minimum at $t \sim 16.4t_0$ on the left. The energy spectrum at $16.4t_0$ on the right, This is the time when the transition into $\left|\Psi^U\right\rangle$ can first be observed.

4.4.1 Landau-Zener approach

The structure of the eigenvalues in fig. 4.12 motivates a closer look at the avoided crossing from $|\Psi^-\rangle$ to $|\Psi^0\rangle$. The Landau-Zener theory provides a possible approach to describe this crossing. It would predict the transitions to happen right at the time when the difference in the eigenenergies is lowest, which is in agreement with the observations. The transition probability would then be given by the Landau-Zener formula, see eq **??**, and depend only on the minimum difference of the eigenenergies ΔE_{min} and the change in time $\frac{dE}{dt}$ of the eigenenergies close to the crossing.

In the following, the first avoided crossing from fig. 4.15 before the penetration is considered. Its transition probability would be expected to have a significant impact on the doublon production. First, the transition probabilities for different U/J are approximately calculated. The time change of the energy difference is treated with linear regression to enable the use of the Landau-Zener formula, see fig. **??**. For the calculation of the transition probability, a constant projectile velocity is again assumed. The regressions are down as shown in fig 4.16 When considering the change in the eigenvalue difference $\frac{d\Delta E}{dt}$, the Landau-Zener formula becomes:

$$P_{-U} = \mathrm{e}^{-\frac{2\pi}{\hbar}\frac{\Delta E_{min}^2}{\frac{1}{2}\left|\frac{d\Delta E}{dt}\right|}} \tag{4.8}$$

When the regression gradients $g(U)$ are used in units of eV/t_0 with $t_0 = \hbar/eV$ and ΔE_{min} is in eV the formula becomes:

$$P_{-U} = \mathrm{e}^{-4\pi\frac{\Delta E_{min}^2}{|g|}}, \tag{4.9}$$

where $\frac{d\Delta E}{dt} = v_0\frac{d\Delta E}{dz_p}$.

Using the regression gradients and averaging for the asymmetry sites for $v_0 =$

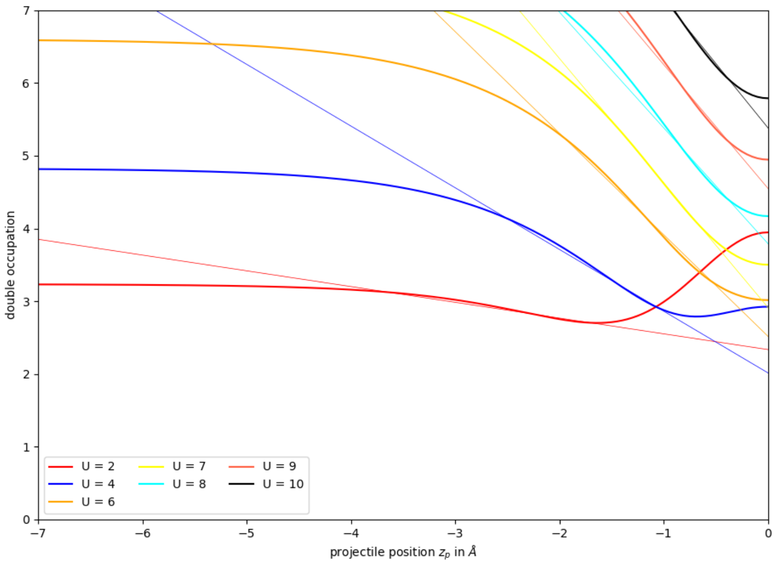

Figure 4.16: $E^U - E^-$ dependent on the projectile position for different U/J with the graphs of the respective linear regression

$4\text{Å}/t_0$ leads to the probabilities shown in fig. 4.17. While the obtained probabilities are too small to explain the doublon production, the dependence on U has a maximum, as is necessary to explain the behaviour of the system. This approach might yield better results when considering both slopes of the crossing, which would lead to higher transition probabilities. Additionally, the second crossing after the projectile has passed the lattice could be considered. This section of the thesis can only be seen as a very basic approach to understanding the occurring dynamics. With more advanced methods, a quantitatively accurate description might be possible.

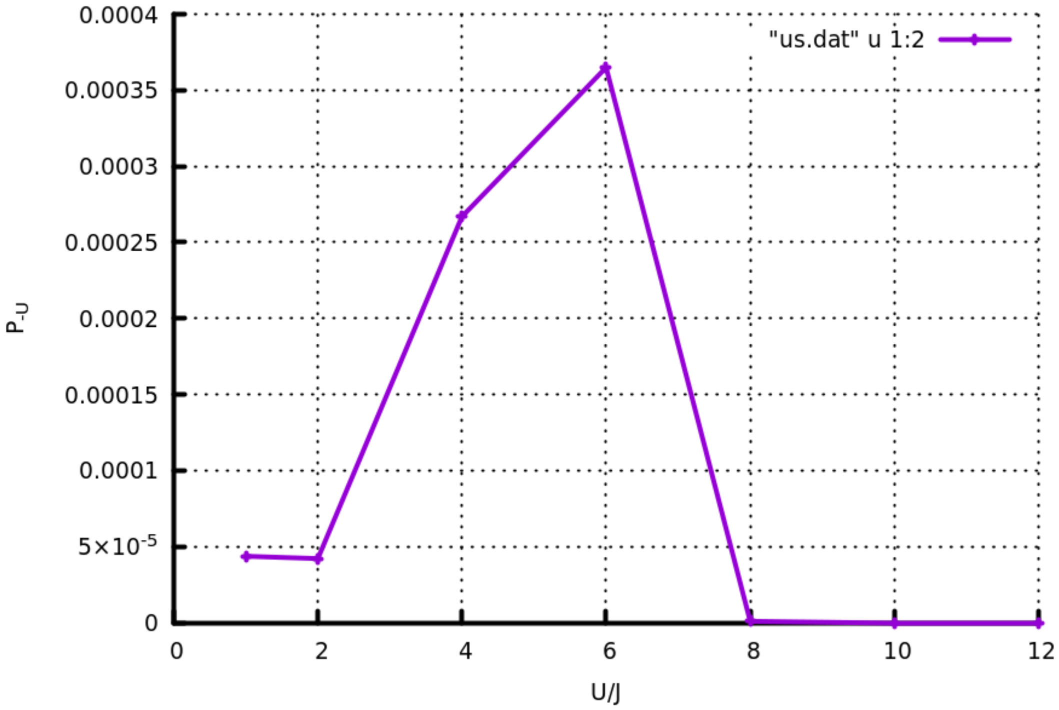

Figure 4.17: comparison of the transition probability and $d_{max} - d_{\mathrm{start}}$ for $v_0 = 10\text{Å}/t_0$

Chapter 5

Conclusions and outlook

In this thesis, the method of exact propagation was used to study the possibility and extent of doublon production in two dimensional honeycomb clusters. The projectile induced dynamics that lead to the creation of doublons in the system were analyzed. The doublons' dissipation speed dependent on the interaction strength was observed and was found to be in good agreement with the theory. The impact of interaction strength, projectile velocity and initial projectile position on the system were observed. The doublon production was found to have a maximum, which depends on interaction strength and projectile velocity. However, this maximum is also highly dependent on the setup symmetry, i.e. initial projectile position. Nevertheless, the area in which the maximum is situated could be roughly determined using the obtained results. On a two site setup that shows qualitatively similar behaviour to the honeycomb lattice, the specific transitions leading to the doublon production could be observed. This offers the opportunity to study the doublon production by directly looking at the important transitions. One possible approach to treat these transitions might be the Landau-Zener formula, which was briefly presented. Although the results obtained with this formula using the most basic methods and inspecting only one possible transition could not explain the behaviour of the system, a more elaborate execution of this theory might lead to much better results.

The data obtained by the simulations done for this thesis can later on be used as a reference when evolving the model further. The next steps in advancing the model could consist of including the possibility of ionization effects and examining the effect of multiple ions penetrating the lattice. With a more extensive model, the importance of doublon creation for plasma surface processes could then be evaluated. Additionally the size of the system could be increased, to study the dissipation of the doublons over more than 12 lattice sites. When moving towards larger systems, the method of non equilibrium green functions could be used, which as already been successfully applied to honeycomb systems of 24 or more sites ([21], [3]).

If, under any circumstances, the local double occupation could be increased without the doublons instantly dissipating all over the system, an experimentally measurable change in the system properties would be predicted. This could, for example, then be experimentally verified by treating materials like graphite or intercalation, which have a quasi two dimensional surface, with plasma and measuring their conductivity.

Bibliography

[1] Assa Auerbach. *Interacting Electrons and Quantum magnetism.* Springer Verlag New York, inc.

[2] Dr. Karsten Balzer. “Calculations concerning particle induced doublons in a 12-site honeycomb lattice.” 2017.

[3] Karsten Balzer, Niclas SchlÃ¼nzen, and Michael Bonitz. “Stopping dynamics of ions passing through correlated honeycomb clusters.” In: *Phys. Rev. B* (2016).

[4] M. Bello, C. E. Creffield, and G. Platero. “Long-range doublon transfer in a dimer chain induced by topology and ac fields.” In: *scientific reports* (2016).

[5] J. P. Biersack. “Computer simulations of sputtering.” In: *Nuclear Instruments and Methods in Physics Research* 27 (1987).

[6] Michael Bonitz. “Quantenstatistik und Quantenfeldtheorie.” 2017.

[7] Lifeng Chen, Peng Bai, and Wenxiu Li. “Preparation of a novel magnesium oxide nanofilm of honeycomb-like structure and investigation of its properties.” In: *Chemical engineering journal* (2016).

[8] C. J. Cramer. *Essentials of computational chemistry: theories and models.* 2013.

[9] James W. Demmel. *Applied Numerical Linear Algebra.* 1997.

[10] Fabian H. L. Essler et al. *The One-Dimensional Hubbard Model.* 1993.

[11] John Hubbard. “Electron correlations in narrow energy bands.” In: *Proceedings of the royal society of london a: mathematical, physical and engineering sciences* (1963).

[12] S. Akbar Jafari. “Introduction to Hubbard Model and Exact Diagonalization.” In: *Iranian J. Phys. Res.* (2008).

[13] JorgePosadaa et al. “In-situ optical emission spectroscopy for a better control of hybrid sputtering/evaporation process for the deposition of Cu(In,Ga)Se2 layers.” In: *Thin Solid Films* (2015).

[14] Jason Lee et al. “Two-Dimensional Pnictogen Honeycomb Lattice: Structure, On-Site Spin Orbit Coupling and Spin Polarization.” In: *nature* (2015).

[15] Gary Z. Li et al. “Implementation of in situ diagnostics for sputter yield measurements in a focused plasma.” In: *Propulsion and Energy Forum* (2016).

[16] A. H. MacDonald, S. M. Girvin, and D. Yoshioka. “t/U expansion for the Hubbard model.” In: *Physical Review Lett.* (1988).

[17] Lukas Oesinghaus. “StabilitÃ¤t und Dynamik von Doublons im Hubbard-Modell.” B.S. Thesis. 2013.

[18] Christopher Paige. “Accuracy and effectiveness of the Lanczos algorithm for the symmetric eigenproblem.” In: *Linear Algebra and its Applications* (1979).

[19] Jan R. Rubbmark et al. “Dynamical effects at aoided level crossings: A study of the Landau Zener effect using Rydberg atoms.” In: *Phys. Review Letters* 23 (1981).

[20] M. SchÃ¼ler et al. “Optimal Hubbard models for materials with nonlocal Coulomb interactions: graphene, silicene and benzene.” In: *Phys. Rev. Lett.* (2013).

[21] Niclas SchlÃ¼nzen. “Nonequilibrium Green functions analysis of electron dynamics in strongly correlated lattice systems.” MA thesis. Christian-Albrechts-UniversitÃ¤t zu Kiel, 2015.

[22] Ulrich Schneider et al. “Fermionic transport in a homogeneous Hubbard model: Out-of-equilibrium dynamics with ultracold atoms.” In: *nature* (2012).

[23] Gary S. Selwyn et al. “In situ plasma contamination measurements by HeNe laser light scattering: A case study.” In: *Journal of Vacuum Science and Technology A* (1990).

[24] H. Tasaki. “The hubbard model - an introduction and selected rigorous results.” In: *J. Phys. Condensed Matter* (1998).

[25] Philip Taylor and Olle Heinonen. *A Quantum Approach to Condensed Matter Physics.* 2002.

[26] “Ultracold quantum gases in three-dimensional optical lattice potentials.” PhD thesis. Ludwig-Maximilians-UniversitÃ¤t MÃ¼nchen, 2003.

[27] S. Zhao et al. “Comparison of electronic energy loss in graphene and BN sheet by means of time-dependent density functional theory.” In: *J. Phys.: Condens. Matter* 27 (2014).

[28] James F. Ziegler, M. D. Ziegler, and J. P. Biersack. “SRIM- The Stopping and Range of Ions in Matter.” In: *Nuclear Instruments and Methods in Physics Research Section B* 68 (2010).

Erklärung

Hiermit erkläre ich, dass ich die vorliegende Arbeit selbstständig und ohne fremde Hilfe angefertigt und keine anderen als die angegebenen Quellen und Hilfsmittel verwendet habe.

Weiterhin versichere ich, dass diese Arbeit noch nicht als Abschlussarbeit an anderer Stelle vorgelegen hat.

Kiel, den 24. August 2017